

# The Co-Moving Velocity in Immiscible Two-Phase Flow in Porous Media

Subhadeep Roy<sup>a</sup>, Håkon Pedersen<sup>a</sup>, Santanu Sinha<sup>a,b</sup>, Alex Hansen<sup>a</sup>

<sup>a</sup>*PoreLab, Department of Physics, Norwegian University of Science and Technology, N-7491 Trondheim, Norway.*

<sup>b</sup>*Beijing Computational Science Research Center, 10 East Xibeiwang Road, Haidian District, Beijing 100193, China.*

---

## Abstract

We present a continuum (i.e., an effective) description of immiscible two-phase flow in porous media characterized by two fields, the pressure and the saturation. Gradients in these two fields are the driving forces that move the immiscible fluids around. The fluids are characterized by two seepage velocity fields, one for each fluid. Following Hansen et al. (Transport in Porous Media, 125, 565 (2018)), we construct a two-way transformation between the velocity couple consisting of the seepage velocity of each fluid, to a velocity couple consisting of the average seepage velocity of both fluids and a new velocity parameter, the co-moving velocity. The co-moving velocity is related but not equal to velocity difference between the two immiscible fluids. The two-way mapping, the mass conservation equation and the constitutive equations for the average seepage velocity and the co-moving velocity form a closed set of equations that determine the flow. There is growing experimental, computational and theoretical evidence that constitutive equation for the average seepage velocity has the form of a power law in the pressure gradient over a wide range of capillary numbers. Through the transformation between the two velocity couples, this constitutive equation may be taken directly into account in the equations describing the flow of each fluid. This is e.g., not possible using relative permeability theory. By reverse engineering relative permeability data from the literature, we construct the constitutive equation for the co-moving velocity. We also calculate the co-moving constitutive equation using a dynamic pore network model over a wide range of parameters, from where the flow is viscosity dominated to where the capillary and viscous forces compete. Both the relative permeability data from the literature and the dynamic pore network model give the same very simple functional form for the constitutive equation over the whole range of parameters.

**Keywords:** two-phase flow, effective rheology, seepage and co-moving velocity, dynamic pore network model, relative permeability.

---

## 1. Introduction

When two immiscible fluids compete for the same pore space, we are dealing with immiscible two-phase flow in porous media [1]. A holy grail in porous media research is to find a proper description of immiscible two-phase flow at the continuum level, i.e., at scales where the porous medium may be treated as a continuum. Our understanding of immiscible two-phase flow at the pore level is increasing at a very high rate due to advances in experimental techniques combined with an explosive growth in computer power [2]. Still, the gap in scales between the physics at the pore level and a continuum description remains huge and the bridges that have been built so far across this gap are either complicated to cross or rather rickety. To the latter class, we find the still dominating theory, first proposed by Wyckoff and Botset in 1936 [3] and with an essential amendment by Leverett in 1940 [4], namely relative permeability theory. The basic idea behind this theory is the following: Put yourself in the place of one of the two immiscible fluids. What does this fluid see? It sees a space in which it can flow limited by the solid matrix of the porous medium, but also by the other fluid. This reduces its mobility in the porous medium by a factor known as the relative permeability for that fluid. And here is the rickety part: this reduction of available space — expressed through the saturation — is assumed to be the *only* parameter affecting the reduction factor or relative permeability.

---

*Email addresses:* subhadeeproy03@gmail.com (Subhadeep Roy), hakon.pedersen@ntnu.no (Håkon Pedersen), santanu.sinha@ntnu.no (Santanu Sinha), alex.hansen@ntnu.no (Alex Hansen)

This is a very strong statement and clearly does not take into account that the distribution and shape of the immiscible fluid clusters will depend on how fast the fluids are flowing, and that these two factors affect the reduction of the permeability. Still, in the range of flow rates relevant for many industrial applications, this assumption works pretty well. It therefore remains the essential work horse for practical applications.

Thermodynamically Constrained Averaging Theory (TCAT) [5–9] is a very different approach to immiscible two-phase flow problem. The TCAT approach is generic and not particular to two-fluid flow problems. It is based on thermodynamically consistent definitions made at the macro-scale based on volume averages of pore-scale thermodynamic quantities. Closure relations are then formulated at the macro-scale along the lines of the homogenization approach of Whittaker [10]. A key advantage of TCAT is that all quantities are explicitly defined in terms of pore-scale quantities. For example, the pressure that appears in Darcy’s law would be formally defined as a volume average of the pore-scale pressure field. A key disadvantage of TCAT is that very many averaged variables are produced, and many complicated assumptions are needed to derive useful results.

Another development somewhat along the same lines, based on non-equilibrium thermodynamics uses Euler homogeneity to define the up-scaled pressure. From this, Kjelstrup et al. derive constitutive equations for the flow [11, 12].

Another class of theories is based on detailed and specific assumptions concerning the physics involved. An example is Local Porosity Theory [13–18]. Another is DeProf (Decomposition in Prototype Flow) theory which is a fluid mechanical model combined with non-equilibrium statistical mechanics based on a classification scheme of fluid configurations at the pore level [19–21].

Recent work [22, 23] has explored a new approach to immiscible two-phase flow in porous media based on Euler homogeneity. It provides a transformation from the seepage velocity of each fluid to another pair of fluid velocities, the average seepage velocity and the *co-moving* velocity. The co-moving velocity, as we shall see, is a velocity parameter that appear as a result of the Euler scaling assumption, which is not associated with any material transport. The transformation is reversible: knowing the average seepage velocity and the co-moving velocity, one can determine the seepage velocity of each fluid. It is the aim of the present work to develop this approach further, especially with respect to the co-moving velocity.

A little more than a decade ago, Tallakstad et al. [24, 25] injected simultaneously air and a glycerol-water mixture into a glass-bead filled Hele-Shaw cell measuring the pressure drop across it as a function of the combined flow rate of the two fluids, finding a power law relation between them. Aursjø et al. [26] repeated the Tallakstad et al. experiment, but this time with two incompressible fluids, finding the same power law dependency, but with a somewhat different power law exponent. The power law relation between pressure difference and flow rate, which corresponds to the local average seepage velocity depending on the local pressure gradient to a power when gradients in the saturation are negligible, has since been reported by other groups, [27–29]. This includes finding that the power law regime exists only in a finite range of pressure gradients; at smaller or larger gradients the relation is linear. Computational and theoretical approaches to understanding this behavior have followed the experimental findings, see [30–37].

This non-linear constitutive law for the average seepage velocity is a reflection of the behavior of each of the two immiscible fluids. The Euler approach of Hansen et al. [22, 23] makes it possible to transform this constitutive law describing the local average seepage velocity as a function of the local driving forces into constitutive laws for each of the two fluids. However, this hinges on providing a constitutive law for the co-moving velocity.

We will in this paper develop a constitutive equation for the co-moving velocity under the assumption that gradients in the saturation may be neglected. Together with the constitutive equation for the average velocity, we then have a complete description of the flow as long as there are no saturation gradients.

Generalizing our results to when there are saturation gradients will be the subject of future investigations.

We investigate the constitutive equation for the co-moving velocity using two approaches. The first one is to use experimental relative permeability data from the literature to construct the constitutive equation for the co-moving velocity. Since the relative permeability approach obeys the Euler homogeneity assumption, it is possible to express the co-moving velocity in terms of the relative permeabilities. This opens up for *reverse engineering* the experimental data which have been cast in

terms of relative permeability curves in order to construct the co-moving velocity.

It should be noted here that this reverse engineering of the data does *not* rely on the relative permeability constitutive equations being accurate or even correct. It simply consists of translating the data that have been cast in the form of relative permeability data into seepage velocity data that in turn allow us to construct the co-moving velocity.

The second approach is based on a dynamic pore network model [38] first introduced by Aker et al. [39] and then later refined [40, 41]. A review of the model was recently published by Sinha et al. [42]. It allows us to emulate closely the experiments of Tallakstad et al. [24, 25], e.g. reproducing the power law dependence of the flow rate on the pressure drop [30].

The constitutive law for the co-moving velocity turns out to be surprisingly simple, see equation (52). The reason for this remains an open question.

The main body of the paper is divided into three sections. The first one, Section 2, reviews the Euler homogeneity approach to immiscible two-phase flow in porous media [22, 23]. The Section starts by laying the groundwork for the theory by defining central variables.

In Subsection 2.1, we address central questions concerning these variables: Are they at all possible to define or will they be swamped by fluctuations? Is it possible to see them as *state variables*, that is, variables that describe the flow there and then without depending on the history of the system? Can we still deal with these variables when there is hysteresis? After this discussion, we go on to describe in Subsection 2.2 the consequences of the volumetric flow rate being an Euler homogeneous function in the area over which the volume is measured. We then go on in Subsection 2.3 describe how the equations of the previous subsection together with constitutive equations for the local average seepage velocity and the local co-moving velocity form a closed set of equations that determine the local seepage velocities of the fluids, the local saturation and the local pressure field. In Subsection 2.4 we give a physical interpretation of the meaning of the co-moving velocity. The next Section 3 we turn to analyzing experimental data from the literature that allow us to reconstruct the co-moving velocity. We start this section by describing (Subsection 3.1) how relative permeability theory may be cast in the language of the Euler scaling approach of Section 2. In this way, we relate the relative permeabilities to the co-moving velocity. We emphasize yet again that this does not imply that relative permeability theory is correct. Rather, the assumption is: If we assume the central equations of relative permeability theory, then the co-moving velocity could be expressed in terms of relative permeability curves, see equations (45) or (46). The next Subsection 3.2 present our analysis of different relative permeability data sets including the reconstructed co-moving velocity, see equation (52). This is the main result in this paper. Section 4 focuses on using a dynamic pore network model to calculate the co-moving velocity. Subsection 4.1 details how we extract the average seepage velocity and then the co-moving velocity from the numerical data generated by the model. We then fit the data to the form (52) in Subsection 4.2, finding excellent agreement. Hansen et al. [22] presented the co-moving velocity gotten by the dynamic pore network model, but using a different set of variables than we use here. Subsection 4.3 discusses the relation between the functional form we find for the co-moving velocity here and the one found in Hansen et al. We have earlier in this introduction described the work of Tallakstad et al. [24, 25] and subsequent workers, where a non-linear relation between average seepage velocity and pressure gradient was uncovered. In Subsection 4.4 we report on what happens to the co-moving velocity when the flow is in the regime. The interesting answer is it does not change character. We then go on to investigate in Subsection 4.5 what happens to the co-moving velocity when the wetting saturation or the non-wetting saturation falls below the threshold for two-phase flow. We see a change in the coefficients describing the co-moving velocity, but not its functional form when the wetting saturation falls below the two-phase flow threshold. However, no such jump is seen at the other threshold. We note that there is hysteresis associated with the low wetting saturation threshold but not with the low non-wetting saturation threshold [43]. Lastly in this section, we discuss the effect of changing the viscosity ratio of the two immiscible fluids on the co-moving velocity, see Subsection 4.6. Finally, we draw our conclusions in Section 5.

## 2. Euler scaling approach

We consider in the following two incompressible and immiscible fluids, one of which more wetting with respect to the pore matrix than the other. We will refer to the first fluid as the wetting fluid and the second one the non-wetting fluid. The viscosity of the wetting fluid is  $\mu_w$  and of the non-wetting fluid  $\mu_n$ .

We consider a porous medium at a scale where it may be viewed as a continuum. This is a scale that is much larger than the pore scale. Whereas at the pore scale concepts such as fluid clusters, interfaces and wetting are central, they are not useful at the continuum scale. Rather, different concepts, and hence variables, should be — and to some degree are — used. This is the viewpoint will retain throughout this section.

This viewpoint has consequences. In this continuum limit, the pores are essentially infinitely small, and so are the fluid interfaces in the pores. Hence, it is no longer fruitful to view the problem as the flow of two immiscible fluids since the key notions that belong to such a description all are closely related to pore-scale concepts. Rather, the two immiscible fluids may be seen acting as a *single* fluid whose rheological properties — for example the effective viscosity — is controlled by two variables, the pressure  $P$  and the wetting saturation  $S_w$ .

There are two driving forces in the continuum limit description that get this single fluid to move: spatial gradients in the pressure,  $\nabla P$  and the saturation,  $\nabla S_w$ . The latter driving force has its origin at the pore level in capillary forces. We may express this driving force in terms of a field with the dimensions of pressure,  $P_c$ , which depends on the saturation, so that  $\nabla P_c(S_w) = (dP/dS_w)\nabla S_w$ . In relative permeability theory, we would call  $P_c$  the dynamic capillary pressure field.

It is necessary to describe the single fluid using *two* velocity fields. This is a reflection of the saturation not being transported at the same velocity as the fluid itself. We name the velocity field that transports the fluid  $\vec{v}_p$  and the velocity field that transports the wetting saturation  $\vec{v}_w$ ,

$$\phi \frac{\partial S_w}{\partial t} = \nabla \cdot \vec{v}_w \phi S_w, \quad (1)$$

where  $\phi$  is the porosity field and  $t$  is time.

We define the porosity field as follows: We may associate with each point in the porous medium a Representative Elementary Volume (REV) which is very large compared to the pore scale, but small compared to continuum scale. The porosity of a given point is then the pore volume of REV divided by the volume of the REV. We note that there might be structure in the porous medium at the continuum scale, so that the porosity field may vary spatially, generating a non-zero gradient  $\nabla \phi$ .

We also define a Representative Elementary Area (REA) [44]. We pick a point in the porous medium. There will be a stream line associated with the velocity field  $\vec{v}_p$  at that point. We place a plane of area  $A$  orthogonal to the stream line centered at the point. We assume that the plane is small enough so that the other stream lines passing through the plane all are essentially parallel to the first one. We also assume that the plane is small enough for the porous medium to be homogeneous over the size of the plane with respect to porosity and permeability. This is the REA.

This allows us to define a transverse pore area

$$A_p = \phi A. \quad (2)$$

The transverse pore area is the area of the REA that cuts through the pores.

The transverse pore area  $A_p$  may be split into a transverse wetting fluid area  $A_w$  and a transverse non-wetting fluid area  $A_n$ . We mean by  $A_w$  the area of the plane covered by the wetting fluid and  $A_n$  the area covered by the non-wetting fluid. We have that

$$A_p = A_w + A_n. \quad (3)$$

The wetting and non-wetting saturations  $S_w$  and  $S_n$  may be expressed as

$$S_w = \frac{A_w}{A_p}, \quad (4)$$

and

$$S_n = \frac{A_n}{A_p}, \quad (5)$$

so that

$$S_w + S_n = 1. \quad (6)$$

There is a volumetric flow rate  $Q_p$  passing through the plane which may be decomposed into a volumetric flow rate for the wetting fluid,  $Q_w$ , and a volumetric flow rate for the non-wetting fluid  $Q_n$ . We have that

$$Q_p = Q_w + Q_n. \quad (7)$$

This allows us to define three velocities,

$$v_w = \frac{Q_w}{A_w}, \quad (8)$$

and

$$v_n = \frac{Q_n}{A_n}, \quad (9)$$

and

$$v_p = \frac{Q_p}{A_p} = \frac{A_w}{A_p} \frac{Q_w}{A_w} + \frac{A_n}{A_p} \frac{Q_n}{A_n} = S_w v_w + S_n v_n. \quad (10)$$

These are the *seepage velocities*. We will refer to  $v_p$  as the *average seepage velocity* in the following.

We may note here that since we are assuming the fluids to be incompressible, it makes no difference whether we define the seepage velocities of each fluid with respect to volume flow or mass flow. However, the average seepage velocity  $v_p$ , defined in equation (10) will be different if averaged with respect to mass rather than volume. The formalism we are about to develop in Section 2.2 and onwards, could have been done using this averaging instead. We have, however, decided to stick with volume averaging.

### 2.1. Fluctuations, state variables and hysteresis

We will in the following sections treat the variables we have just defined as functions of each other, even to the point of taking derivatives. In this section, we pose the question of whether this is at all possible. There are three aspects we need to address in this context: The first one concerns *fluctuations*. If the variables we consider fluctuate strongly, it is not possible to find functional relations between them. The second aspect is the question of whether the variables we measure depend only on the flow there and then or whether they in addition depend on the history of the flow. If the former is true, we are dealing with *state variables*. The third aspect concerns the possibility of these variables being multi-valued. That is, there is *hysteresis*. Is the analysis we present still valid when there is hysteresis?

*Fluctuations:* Self-averaging is an important property of fluctuating systems. A self-averaging system is one where the relative strength of the fluctuations shrinks with increasing size of the system. If this is so, the variables attain well-defined values and functional relations between them may be sought.

To give an example, this is precisely the situation when thermodynamics is used to describe a gas. The more molecules it consists of, the more well defined the macroscopic thermodynamic variables and their relations are. We note, however, that in such systems there is one exception: At critical points, the fluctuations dominate and self-averaging is lost [45].

An important feature of flooding processes, slow or fast, is that they typically generate fractal injection patterns [46]. These patterns, like the fluctuations near critical points, are typically not self-averaging. However, there will always be a largest length scale above which the process does not produce fractals. Here, self-averaging sets in. In the continuum limit — which is what we consider here — we are surely above this scale.

It should be noted that there is not a one-to-one correspondence between the fluid configurations and the values of the macroscopic variables. Rather, typically there are many fluid configurations giving rise to the same values for the macroscopic variables. This is not a problem as it is the macroscopic variables that are measured, not the underlying fluid configurations.

One may then ask oneself, does this mean that the theory being developed here is untestable on small systems such as those that can be modeled using computational method such as the lattice Boltzmann method or dynamic pore network models since we can never reach sufficient system sizes for the fluctuations to be small enough? The answer is no as one may use time averaging to emulate size. In fact, Kjelstrup et al. [11] report that around 100 links are enough to define a REV in the dynamic pore network model [42] we explore further on in this paper.

*State variables:* Steady-state flow of immiscible fluids in a porous medium needs to be carefully defined. We have settled on the following: It is a flow where the macroscopic variables have values (measured in practice as gliding averages over time) that do not drift in any direction. This does not preclude fluid clusters moving, merging and breaking up. In three-dimensional flow, one may have that both fluid phases percolate. If the flow then is not too fast, the fluid interfaces will not move. However, when there is no percolation of either phase, which is typically easier to obtain in two-dimensional systems, the clusters will exhibit a rich dynamics.

Erpelding et al. [47] studied experimentally and computationally such a two-dimensional system. Their experimental set-up consisted of a two-dimensional (42 cm  $\times$  85 cm) Hele-Shaw cell filled with immobilized 1 mm glass beads. Along one of the short edge, two immiscible fluids (a water-glycerol mixture and air) were injected simultaneously through 15 alternating injection points at constant rates. The opposite edge of the Hele-Shaw cell was left open, and the two orthogonal sides were both sealed. Hence, there would be a flow across the cell from the injection points in the direction of the open edge. Some distance from the injection points in the flow direction, the fluids would mix sufficiently to create a mixture of fluid clusters that when averaged over time would be homogeneous.

This system would be set up at a given flow rate and a number of variables were measured. The flow rate would then be raised and new values for the variables would be measured. Then, the flow rate would revert to the original value and the variables measured anew. The variables would attain the values they had before the flow rate was raised. The flow is *history independent* in the language of Erpelding et al. [47], and the macroscopic variables describing it would then be *state variables*. They would characterize the flow there and then, and not depend on the history of the flow.

*Hysteresis:* There is the hysteresis caused by the difference between first and secondary flooding [2]. Typically at low injection rates, the system will remember its history and the values for the macroscopic variables will be different when the first and second time one floods the system.

There is, however, also another kind of hysteresis which is related to the study of Erpelding et al. [47]. Modeling the Hele-Shaw system, Knudsen and Hansen [43] studied the wetting fractional flow as function of wetting saturation under steady-state conditions using a dynamic pore network model. They found that there are two transitions between two-phase flow and single-phase flow when the saturation is the control parameter. The transition between only the non-wetting fluid moving at low saturation to both fluids moving at higher saturation does not show any hysteresis with respect to which way one passes through the transition. However, the other transition between only the wetting fluid moving at high saturation and both fluids moving at lower saturation does show a strong hysteresis. This is depicted in Figure 2 in Reference [43]. This hysteresis, we believe, is caused by this transition being related to a first order (or spinodal) phase transition.

Hysteretic behavior is a signal that the macroscopic state variables are multi-valued, signaling — of course — that the underlying microscopic physics has more than one stable mode. Hysteresis is far from uncommon in physics. In fact, it is a defining property of first order phase transitions. There are no principal problems manipulating multi-valued functions, for example taking their derivatives as long as one does not mix up the branches.

## 2.2. Homogeneity of $Q_p$ and consequences thereof

In the following we review the central arguments in [22].

The volumetric flow rate  $Q_p$  across the REA is a homogeneous function of order one in the transverse area variables  $A_w$  and  $A_n$ . That is,

$$Q_p(\lambda A_w, \lambda A_n) = \lambda Q_p(A_w, A_n), \quad (11)$$

where  $\lambda$  is a scale factor. Taking the derivative with respect to  $\lambda$  and setting  $\lambda = 1$  in this expression, we get,

$$Q_p(A_w, A_n) = A_w \left( \frac{\partial Q_p}{\partial A_w} \right)_{A_n} + A_n \left( \frac{\partial Q_p}{\partial A_n} \right)_{A_w} . \quad (12)$$

Dividing  $Q_p$  in this equation by the transverse pore area  $A_p$ , we get

$$v_p = S_w \left( \frac{\partial Q_p}{\partial A_w} \right)_{A_n} + S_n \left( \frac{\partial Q_p}{\partial A_n} \right)_{A_w} = S_w \hat{v}_w + S_n \hat{v}_n . \quad (13)$$

where

$$\hat{v}_w = \left( \frac{\partial Q_p}{\partial A_w} \right)_{A_n} , \quad (14)$$

and

$$\hat{v}_n = \left( \frac{\partial Q_p}{\partial A_n} \right)_{A_w} , \quad (15)$$

are the *thermodynamic velocities*. They differ from the seepage velocities (8) and (9) as we shall see, this in spite of  $v_p$  being given by both (10) and (13).

We may express the two thermodynamic velocities  $\hat{v}_w$  and  $\hat{v}_n$  in terms of the average seepage velocity  $v_p$ . In order to do so, we change our control variables from  $(A_w, A_n)$  to  $(A_p, S_w)$ . We use equations (4) and (5) and the chain rule to derive

$$\left( \frac{\partial}{\partial A_w} \right)_{A_n} = \frac{S_n}{A_p} \left( \frac{\partial}{\partial S_w} \right)_{A_p} + \left( \frac{\partial}{\partial A_p} \right)_{S_w} , \quad (16)$$

and

$$\left( \frac{\partial}{\partial A_n} \right)_{A_w} = -\frac{S_w}{A_p} \left( \frac{\partial}{\partial S_w} \right)_{A_p} + \left( \frac{\partial}{\partial A_p} \right)_{S_w} . \quad (17)$$

We now combine these two equations with the definitions (14) and (15), and use  $Q_p = A_p v_p$ , i.e. equation (10), to find

$$\hat{v}_w = v_p + S_n \frac{dv_p}{dS_w} , \quad (18)$$

and

$$\hat{v}_n = v_p - S_w \frac{dv_p}{dS_w} . \quad (19)$$

This is a remarkable result in that  $\hat{v}_w$  and  $\hat{v}_n$  are fully determined by  $v_p$  and its derivative with respect to  $S_w$ . In other words, it is enough to know  $v_p(S_w)$  to determine *both*  $\hat{v}_w$  and  $\hat{v}_n$ .

From equations (10) and (13), we have that

$$S_w v_w + S_n v_n = S_w \hat{v}_w + S_n \hat{v}_n . \quad (20)$$

The most general relation between between  $(\hat{v}_w, \hat{v}_n)$  and  $(v_w, v_n)$  is given by the pair of equations

$$\hat{v}_w = v_w + S_n v_m , \quad (21)$$

and

$$\hat{v}_n = v_n - S_w v_m , \quad (22)$$

where a new velocity function  $v_m$  has been introduced. This is the *co-moving velocity*.

Equations (21) and (22) *define* the co-moving velocity. The co-moving velocity provides the link between the seepage velocities and the thermodynamic velocities.



We combine the two equations (21) and (22) with equations (18) and (19), to find

$$v_w = v_p + S_n \left( \frac{dv_p}{dS_w} - v_m \right) , \quad (23)$$

and

$$v_n = v_p - S_w \left( \frac{dv_p}{dS_w} - v_m \right) . \quad (24)$$

Thus, we have expressed the seepage velocity for each fluid  $v_w$  and  $v_n$  in terms of the average seepage velocity  $v_p$  and the co-moving velocity  $v_m$ . This is in contrast to the thermodynamic velocities  $\hat{v}_w$  and  $\hat{v}_n$  where only the average seepage velocity  $v_p$  was needed, see equations (18) and (19).

We may see equations (18) and (19) as a mapping  $(v_p, v_m) \rightarrow (v_w, v_n)$ . The couple  $(v_p, v_m)$  contains the same information as the couple  $(v_w, v_n)$ .

The co-moving velocity was defined in equations (21) and (22). We may express it explicitly by solving (23) and (24) with respect to  $v_m$ , finding

$$v_m = \frac{dv_p}{dS_w} + (v_n - v_w) . \quad (25)$$

If we now take the derivative of equation (10) with respect to  $S_w$  and combine the resulting equation with equation (25), we find

$$v_m = S_w \frac{dv_w}{dS_w} + S_n \frac{dv_n}{dS_w} . \quad (26)$$

We may take either of equations (25) and (26) as alternative definitions of the co-moving velocity.

For clarity, we now display equations (10) and (26) together as follows:

$$\begin{aligned} v_p &= S_w v_w + S_n v_n , \\ v_m &= S_w v'_w + S_n v'_n , \end{aligned}$$

where we have used the notation  $v'_w = dv_w/dS_w$  and  $v'_n = dv_n/dS_w$ . These two equations, (10) and (26), give us the reverse transformation  $(v_w, v_n) \rightarrow (v_p, v_m)$ .

### 2.3. Closed set of equations

We defined the Representative Elementary Area in Section 2. Its size was determined by the largest transverse area over which the streamlines could be regarded as parallel. On larger scales, the stream lines form patterns that reflect the structure and boundaries of the porous medium; e.g., a reservoir. In this Section, we construct a closed set of equations that determine the flow at these scales based on the formalism constructed in the previous Section, conservation laws and constitute equations.

The plane with area  $A$  we introduced in the preceding sub-section was oriented orthogonally to the stream line for  $v_p$  at the point it sits. We may orient it differently generating the same equations, but with the velocities now being components relative to the axis of the new plane. This makes it possible to express the equations in terms of vectors.

The fluids are incompressive so that

$$\nabla \cdot \phi \vec{v}_p = 0 . \quad (27)$$

We have here assumed that the porosity may not be spatially uniform. The continuity equation for the wetting saturation,  $S_w$ , equation (1), may be combined with the vector version of equation (23) to give

$$\phi \frac{\partial S_w}{\partial t} = \nabla \cdot \left[ \vec{v}_p + S_n \left( \frac{d\vec{v}_p}{dS_w} - \vec{v}_m \right) \right] \phi S_w . \quad (28)$$



These two continuity equations must be supplied with two constitutive equations

$$\vec{v}_p = \vec{v}_p(S_w, \nabla S_w, \nabla P), \quad (29)$$

and

$$\vec{v}_m = \vec{v}_m(S_w, \nabla S_w, \nabla P), \quad (30)$$

to produce a closed set of equations that together with the proper boundary and initial values solves the immiscible two-phase flow problem in the continuum limit.

We note that the non-linear constitutive equation that can be constructed for  $\vec{v}_p$  from the observations in [24–29], is easily combined with this approach.

#### 2.4. Interpreting the co-moving velocity $v_m$

Let us now pose the question: is  $\vec{v}_m$  transporting anything? Equations (8), (9) and (10) show that there is volumetric transport associated with the velocities  $\vec{v}_w$ ,  $\vec{v}_n$  and  $\vec{v}_p$ . We will in the following show that there is no such transport associated with  $\vec{v}_m$ .

We base the discussion that now follows on [23]. We will consider components rather than vectors. We introduce the *differential transverse area distributions*  $a_p$ ,  $a_w$  and  $a_n$ . Their meaning is as follows:  $a_p(v)dv$  is the area covered by fluid, wetting or non-wetting, that has a velocity in the interval  $[v, v + dv]$ . Likewise,  $a_w(v)dv$  is the area covered by wetting fluid that has a velocity in the interval  $[v, v + dv]$  and  $a_n(v)dv$  is the area covered by non-wetting fluid that has a velocity in the interval  $[v, v + dv]$ . Hence, we have that

$$A_p = \int_{-\infty}^{\infty} dv a_p, \quad (31)$$

$$A_w = \int_{-\infty}^{\infty} dv a_w, \quad (32)$$

and

$$A_n = \int_{-\infty}^{\infty} dv a_n. \quad (33)$$

The velocities defined in equations (8), (9) and (10) are then given by

$$v_p = \frac{1}{A_p} \int_{-\infty}^{\infty} v dv a_p, \quad (34)$$

$$v_w = \frac{1}{A_w} \int_{-\infty}^{\infty} v dv a_w, \quad (35)$$

and

$$v_n = \frac{1}{A_n} \int_{-\infty}^{\infty} v dv a_n. \quad (36)$$

The differential transverse areas are essentially velocity histograms, thus making a connection between the continuum scale and the flow at small scales.

We may now combine these three equations, (34), (35) and (36), with equation (25) to give

$$v_m = \frac{dv_p}{dS_w} - v_w + v_n = \frac{1}{A_p} \int_{-\infty}^{\infty} v dv \left[ \frac{\partial a_p}{\partial S_w} - \frac{a_w}{S_w} + \frac{a_n}{S_n} \right] = \frac{1}{A_p} \int_{-\infty}^{\infty} v dv a_m, \quad (37)$$

from which we infer

$$a_m(v) = \frac{\partial a_p(v)}{\partial S_w} - \frac{a_w(v)}{S_w} + \frac{a_n(v)}{S_n}. \quad (38)$$

This is the co-moving differential transverse area. We now integrate this over all velocities to find the total co-moving transverse area  $A_m$ ,

$$\begin{aligned} A_m &= \int_{-\infty}^{\infty} dv a_m = \frac{d}{dS_w} \int_{-\infty}^{\infty} dv a_p - \frac{1}{S_w} \int_{-\infty}^{\infty} dv a_w + \frac{1}{S_n} \int_{-\infty}^{\infty} dv a_n \\ &= \frac{dA_p}{dS_w} - \frac{A_w}{S_w} + \frac{A_n}{S_n} = 0. \end{aligned} \quad (39)$$

There is no area associated with the co-moving velocity. As a consequence, there is no volumetric flux associated with it as

$$Q_m = A_m v_m = 0. \quad (40)$$

Both of these results make sense, since  $A_w + A_n = A_p$  (equation (3)) and  $Q_w + Q_n = Q_p$  (equation (7)): There is no room for  $v_m$  being associated with any transverse area or with volumetric transport. We may see the transformation  $(v_w, v_n) \rightarrow (v_p, v_m)$  as a way of partitioning the flow.  $(A_w, A_n)$  and  $(Q_w, Q_n)$  constitute one partitioning,  $(A_p, A_m) = (A_p, 0)$  and  $(Q_p, Q_m) = (Q_p, 0)$  another.

Equation (25) shows that  $v_m$  is related to the relative velocity of the two fluids,  $v_n - v_w$ . However, the difference velocity,  $v_n - v_w$  cannot be given an interpretation as being part of a partitioning of the flow.

Before we now switch to the structure of the co-moving velocity  $v_m$ , it is now appropriate to remind the reader of why the mapping  $(v_w, v_n) \rightleftharpoons (v_p, v_m)$ , that is equations (10) and (26) for the transformation  $(v_w, v_n) \rightarrow (v_p, v_m)$ , and equations (23) and (24) for the transformation  $(v_w, v_n) \leftarrow (v_p, v_m)$ , is important. With the non-linear constitute law for  $v_p$  being uncovered experimentally, computationally and theoretically [24–37], a theory that can relate this constitutive law to the flow properties of each of the immiscible fluids is necessary. It is precisely such a theory that we are presenting here.

### 3. Reverse engineering relative permeability data

Our aim is now to *reverse engineer* experimental data from the literature that have been presented as relative permeability curves to reconstruct a constitutive equation for the co-moving velocity.

In order to do so, we begin this section by placing relative permeability theory within the framework of the Euler homogeneity approach. This allows us to express the co-moving velocity  $v_m$  in terms of the relative permeabilities.

It is important to note here that this approach does not hinge on whether the relative permeability approach is correct or not. Rather, we are simply translating the data back to their origin and from there we construct  $v_m$ .

Which relative permeability data sets to choose? Since we have no preconceived ideas of the form of  $v_m$  or what controls it, we have more or less randomly picked relative permeability data sets. Any other way of picking them would bias the results.

We note that the relative permeability data are hysteretic. There is, however, no problem in taking the derivatives of these curves in order to extract the co-moving velocities. It might be that the co-moving velocities also are hysteretic. At this point, we do not know.

#### 3.1. Relative permeability theory in light of Euler homogeneity

Relative permeability theory [3] is based on the two constitutive equations,

$$\vec{v}_w = -\frac{Kk_{rw}}{\phi S_w \mu_w} \nabla P, \quad (41)$$

and

$$\vec{v}_n = -\frac{Kk_{rn}}{\phi S_n \mu_n} \nabla P, \quad (42)$$

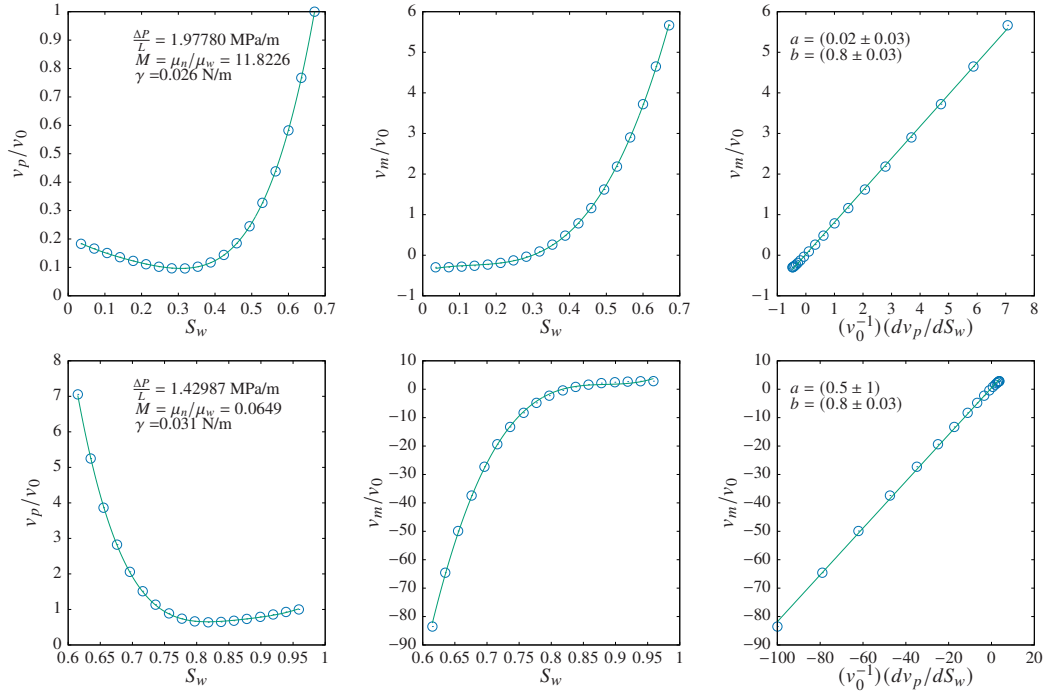


Figure 1: Experimental data from Table 3 in Bennion et al. [49]. Upper row: Basal Cambrian sandstone, drainage with brine as non-wetting fluid and  $\text{CO}_2$  as wetting fluid,  $\phi = 0.177$ ,  $K = 5.43 \times 10^{-16} \text{ m}^2$ . Lower row: Wabamum carbonate, drainage with  $\text{CO}_2$  as non-wetting fluid and brine as wetting fluid,  $\phi = 0.177$ ,  $K = 2.07 \times 10^{-16} \text{ m}^2$ .

when we assume that there are no saturation gradients so that  $\nabla P_c = 0$  [48]. Here  $K$  is the absolute permeability. The factors  $k_{rw} = k_{rw}(S_w)$  and  $k_{rn} = k_{rn}(S_w)$  are the wetting and non-wetting relative permeabilities.

We introduce the plate of area  $A$  as in Section 2.2 and form the volumetric flow rate through it,  $Q_p$ . From this we get  $v_p$  by using equation (10). Combining this equation with the the relative permeability constitutive equations, also named the generalized Darcy equations (41) and (42) gives

$$v_p = -\mu_w v_0 \left[ \frac{k_{rw}}{\mu_w} + \frac{k_{rn}}{\mu_n} \right], \quad (43)$$

where we have introduced a velocity scale which is independent of  $S_w$ ,

$$v_0 = -\frac{K}{\mu_w \phi} |\nabla P|. \quad (44)$$

We see that this is an Euler homogeneous function of order zero in  $A_w$  and  $A_n$  implying that  $Q_p = (A_w + A_n)v_p$  trivially fulfills equation (11). Hence, relative permeability theory obeys all the relations we derive in Section 2.2.

We now combine the generalized Darcy equations (41) and (42) with equation (26) for the co-moving velocity  $v_m$ . We find

$$v_m = \mu_w v_0 \left[ \frac{S_w}{\mu_w} \frac{d}{dS_w} \left( \frac{k_{rw}}{S_w} \right) + \frac{S_n}{\mu_n} \frac{d}{dS_w} \left( \frac{k_{rn}}{S_n} \right) \right]. \quad (45)$$

We may also write  $v_m$  as

$$v_m = \frac{dv_p}{dS_w} + \mu_w v_0 \left[ \frac{k_{rn}}{\mu_n} - \frac{k_{rw}}{\mu_w} \right], \quad (46)$$

using equation (25).

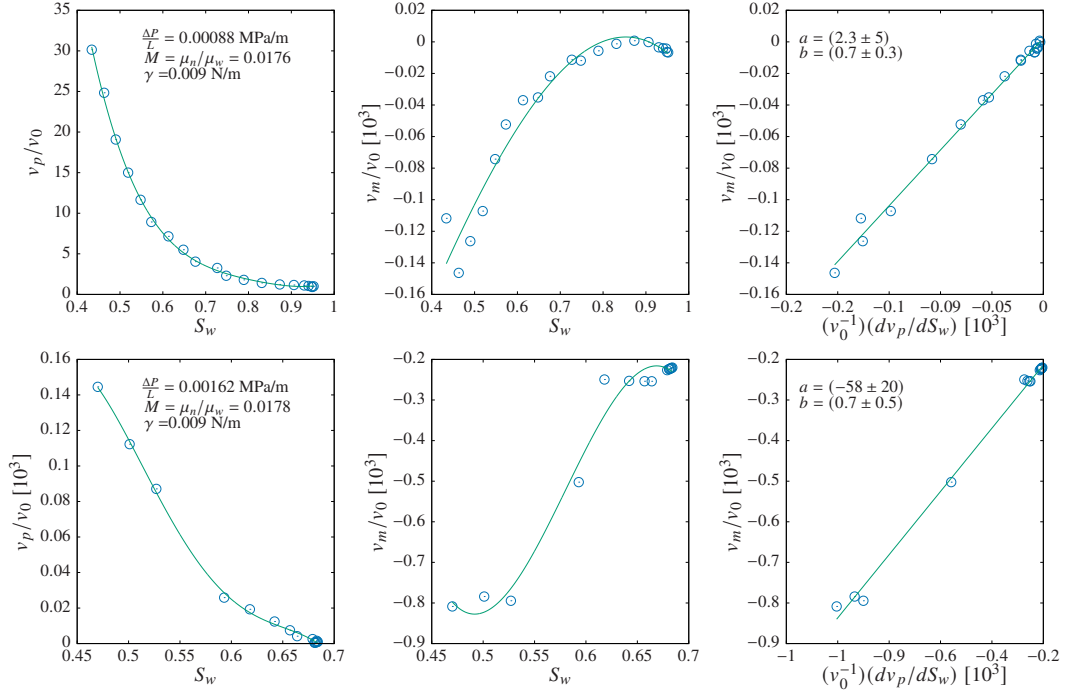


Figure 2: Experimental data from figure 4 in Oak et al. [51]. The process is primary drainage (upper row) and imbibition (lower row) of a single experimental run. Both rows: Berea sandstone, natural gas as non-wetting fluid and water as wetting fluid,  $\phi = 0.193$ ,  $K = 2072.49 \times 10^{-16}$  m<sup>2</sup>.  $\phi$  and  $\gamma$  were not supplied by the authors.

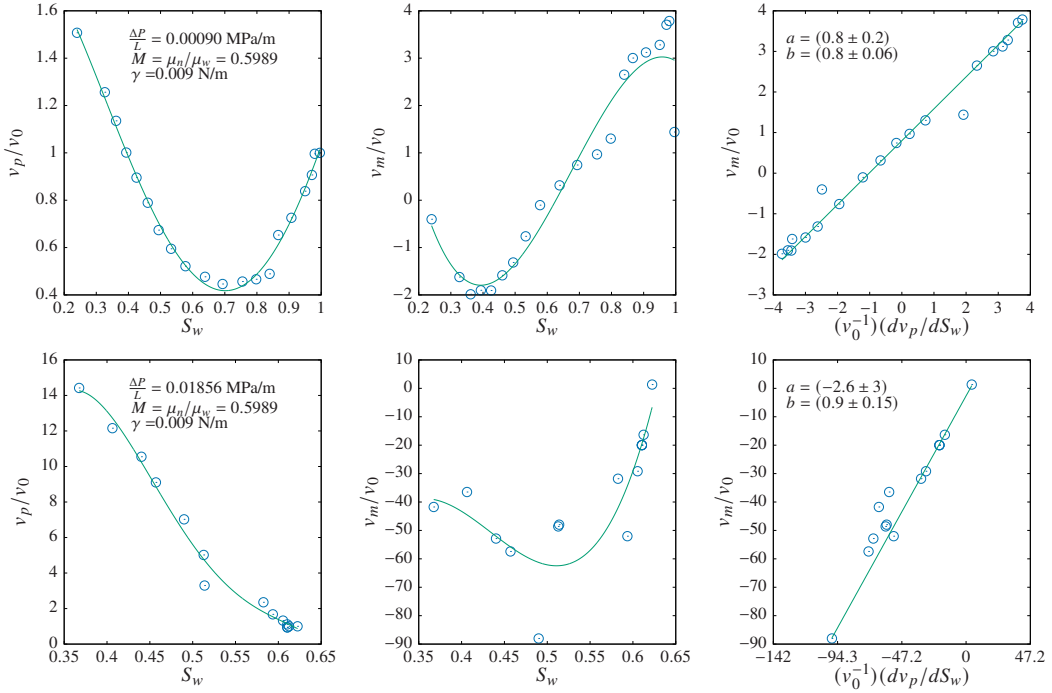


Figure 3: Experimental data from figure 3 in Oak et al. [51]. The process is primary drainage (upper row) and imbibition (lower row) of a single experimental run. Both rows: Berea sandstone, water as non-wetting fluid and oil as wetting fluid,  $\phi = 0.193$ ,  $K = 1973.8 \times 10^{-16}$  m<sup>2</sup>.  $\phi$  and  $\gamma$  were not supplied by the authors.

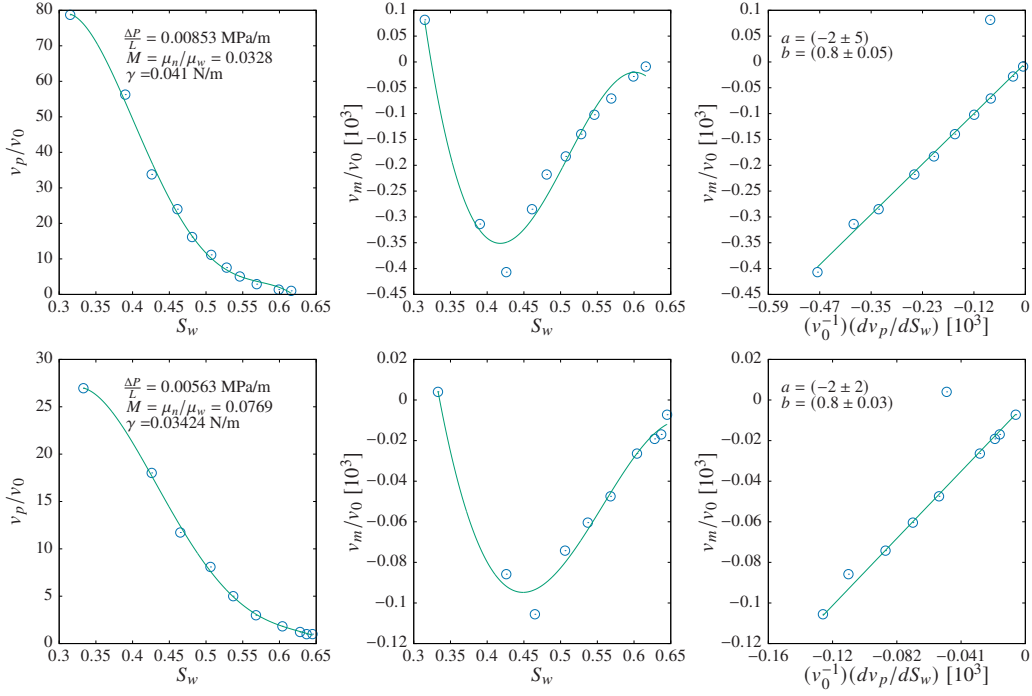


Figure 4: Experimental data from runs no. 4 and 5 in Reynolds et al. [53]. Upper row: Bentheimer sandstone, drainage with CO<sub>2</sub> as non-wetting fluid and water as wetting fluid,  $\phi = 0.222$ ,  $K = 17862.89 \times 10^{-16}$  m<sup>2</sup>. Lower row: Bentheimer sandstone, drainage with CO<sub>2</sub> as non-wetting fluid and brine as wetting fluid,  $\phi = 0.222$ ,  $K = 17862.89 \times 10^{-16}$  m<sup>2</sup>.

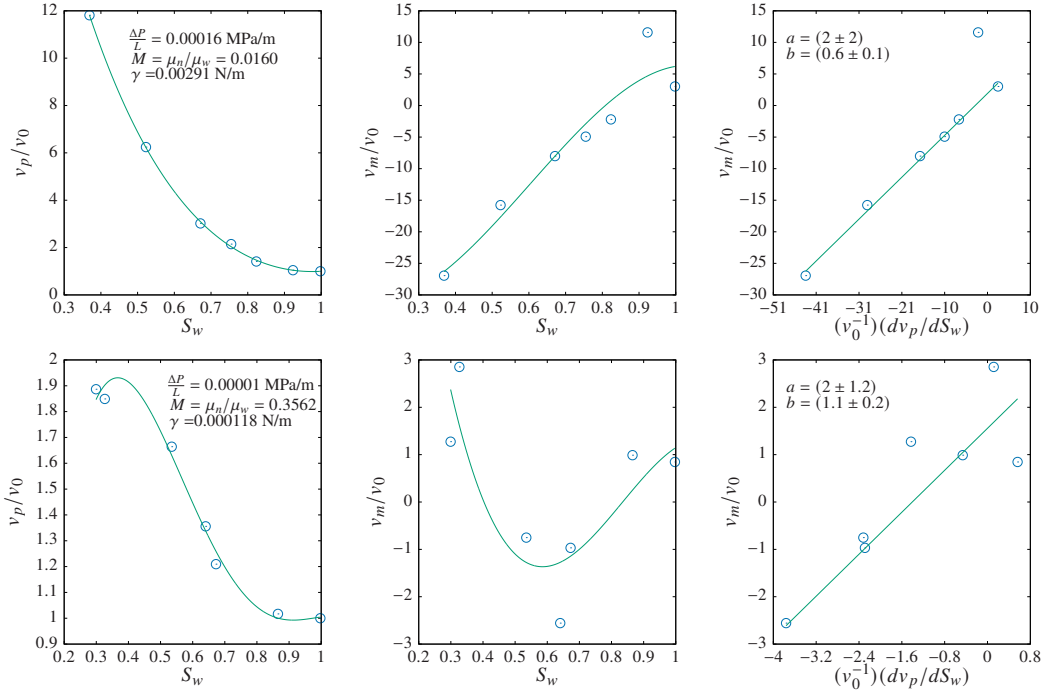


Figure 5: Experimental data extracted graphically using Webplotdigitizer [55] from runs no. 18 and 19 in Fulcher et al. [50]. Both rows: Berea sandstone, drainage with oil as non-wetting fluid and water as wetting fluid,  $\phi = 0.224$ . Upper row has  $K = 4109.45 \times 10^{-16}$  m<sup>2</sup>, and lower row  $K = 3794.63 \times 10^{-16}$  m<sup>2</sup>.

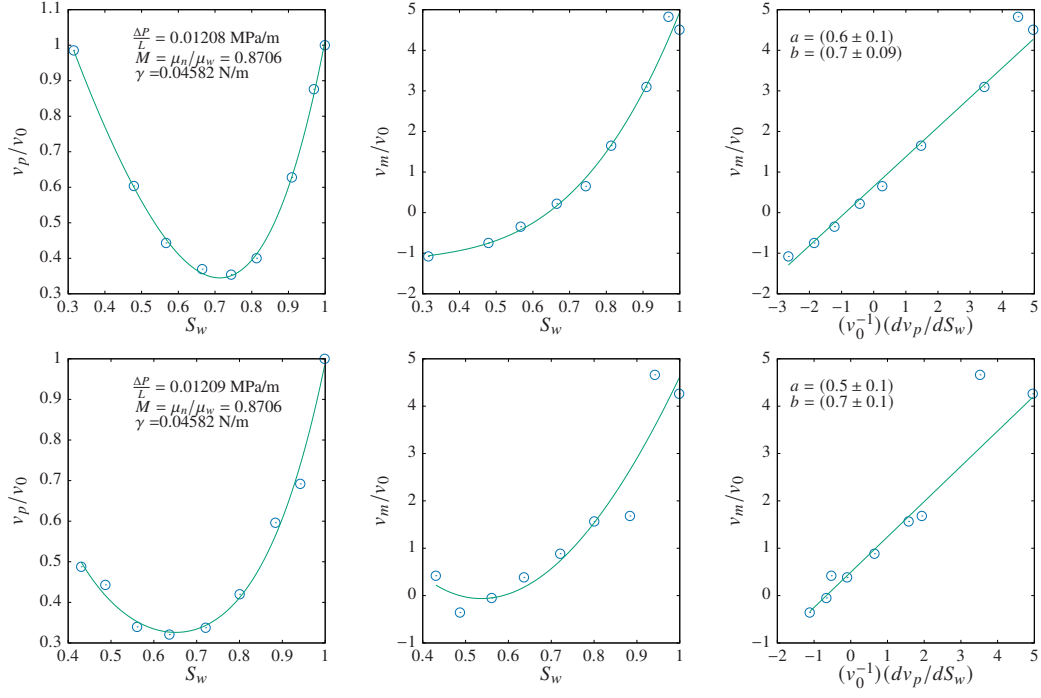


Figure 6: Experimental data extracted graphically from Virnovsky et.al. [52], fig. 4 and 5. Both rows: Berea sandstone, drainage with oil as non-wetting fluid and H<sub>2</sub>O as wetting fluid,  $\phi = 0.561$ ,  $K = 2131.7 \times 10^{-16} \text{ m}^2$ .

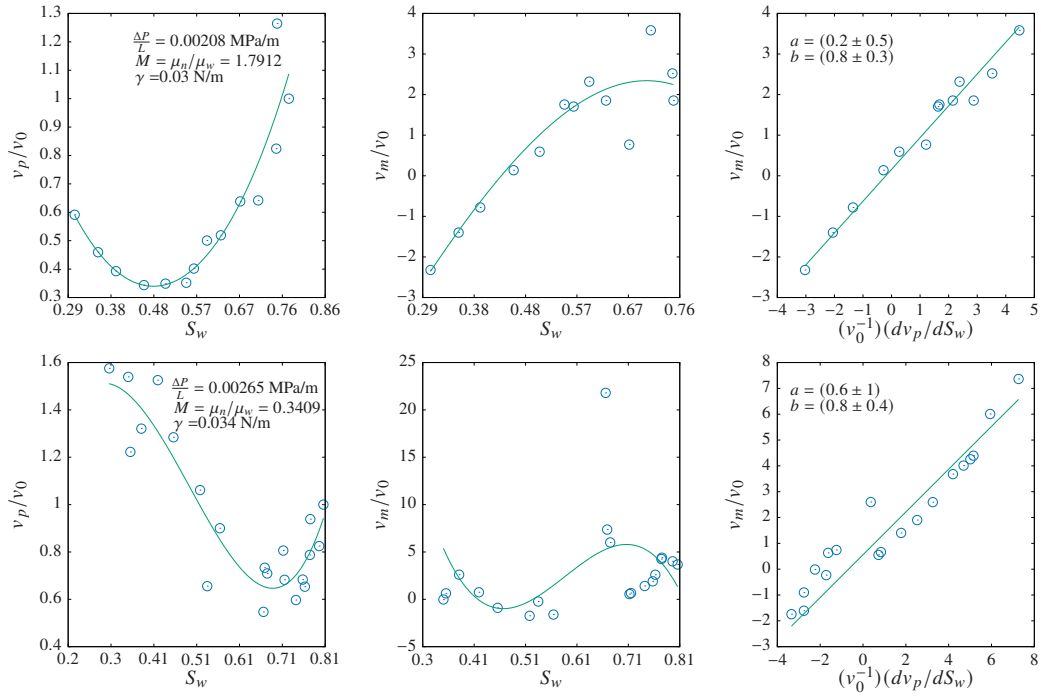


Figure 7: Experimental data extracted graphically using Webplotdigitizer [55] from figure 9 (sand II) in Leverett [54]. Upper row: drainage in sand, with oil as the non-wetting fluid and water as the wetting fluid,  $\phi = 0.35$ ,  $K = 17270.75 \times 10^{-16} \text{ m}^2$ . Lower row: sand with oil as the non-wetting fluid and water as the wetting fluid,  $\phi = 0.45$ ,  $K = 10263.76 \times 10^{-16} \text{ m}^2$ .

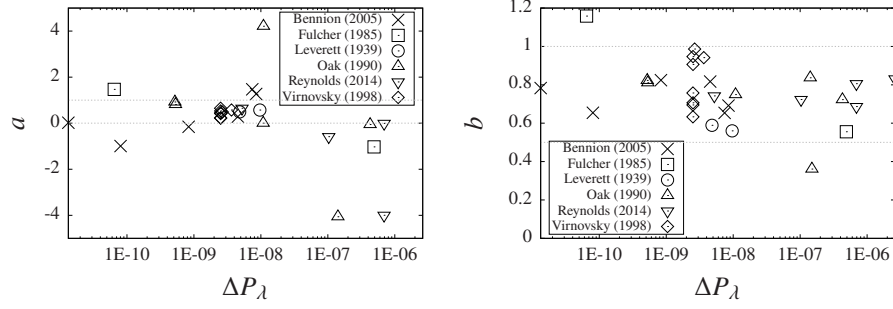


Figure 8: Calculated coefficients  $a$  and  $b$  from all experimental data as a function of the scaled pressure gradient  $\Delta P_\lambda$ . In the left plot, the only data point not shown is  $a = -58 \pm 20$  from the Oak et al. data set [51]. In the right plot, the single data point above  $b = 1$  is obtained from a data set with few data points, see figure 5. Values for more data sets than have been plotted in figures 1 – 7 are included: the rest of the data series in Table 3 in Bennion et al. [49], an additional water/oil data series from figure 3 in Oak et al. [51], runs no. 2, 3 and 6 from Reynolds et al. [53], and the two lower flow-rate data series from figures 4 and 5 in Virnovsky et al. [52].

### 3.2. Analysis of relative permeability curves from the literature

We analyze in the following relative permeability curves from References [49–54] in light of the discussion in Section 3.1. Our aim is to determine  $v_p$  and  $v_m$  as a function of the wetting saturation  $S_w$ .

The wetting and non-wetting relative permeabilities  $k_{rw}(S_w)$  and  $k_{rn}(S_w)$  data together with the wetting and non-wetting viscosities  $\mu_w$  and  $\mu_n$  as supplied by the authors are the essential data we use in our analysis. Other parameters such as the surface tension  $\gamma$ , porosity  $\phi$  and absolute permeability  $K$  we use to set the velocity scale  $v_0$  and to determine a scale for the pressure gradient.

The data points for  $k_{rn}$ ,  $k_{rw}$  and  $S_w$  were obtained explicitly from tables when available in the cited works. If explicit values were not given, the values were extracted graphically from the plots using the software Webplotdigitizer [55].

In all of the experiments, the measurements were performed when the flow reached steady state i.e. when the variation in pressure and saturation attained values within some acceptable threshold interval. The sources have different definitions of when steady state has been reached, but this threshold is usually taken to be fluctuations within 1 – 2% over the span of minutes to hours depending on the experiment, see [51].

The data we use were obtained either during drainage or imbibition processes.

We plot the velocities  $v_p$  in equation (43) and  $v_m$  in equation (45) in dimensionless units by dividing by a velocity scale  $v_0$  and  $\mu_w$ . We do this in the following way: We define

$$\tilde{v}_p(S_w) = \left[ \frac{k_{rw}(S_w)}{\mu_w} + \frac{k_{rn}(S_w)}{\mu_n} \right], \quad (47)$$

and

$$\tilde{v}_m(S_w) = \left[ \frac{S_w}{\mu_w} \frac{d}{dS_w} \left( \frac{k_{rw}(S_w)}{S_w} \right) + \frac{S_n}{\mu_n} \frac{d}{dS_w} \left( \frac{k_{rn}(S_w)}{S_n} \right) \right]. \quad (48)$$

We then define

$$\tilde{v}_0 = \tilde{v}_p(S_w = 1), \quad (49)$$

leading to

$$\frac{v_p(S_w)}{v_0} = \frac{\tilde{v}_p(S_w)}{\tilde{v}_0}, \quad (50)$$

and

$$\frac{v_m(S_w)}{v_0} = \frac{\tilde{v}_m(S_w)}{\tilde{v}_0}. \quad (51)$$

It is the right hand side of these two equations that we plot.



The first and second columns of figures where we present our data analysis 1 — 7 show plots of  $v_p(S_w)/v_0$  and  $v_m(S_w)/v_0$  while the third column shows  $v_m/v_0$  plotted against  $d(v_p/v_0)/dS_w$ . We have used both equations (45) and (46) to determine  $v_m$ . They are of course in principle equivalent, but they demand different numerical differentiations. Both gave the same result. It is the values of  $v_m$  calculated from equation (46) that are shown in the plots.

The experimental data shown in the plots in this section have not been picked based on any special criteria. However, we have prioritized data sets with a larger number of data points for the plots.

We now turn to the results of our analysis. The third column of figures 1 — 7 shows  $v_m/v_0$  as a function of  $v'_p/v_0$  where  $v'_p = dv_p/dS_w$ . The surprising result is that the relation

$$v_m = av_0 + b \frac{dv_p}{dS_w}, \quad (52)$$

where  $a$  and  $b$  are constants with respect to  $v'_p$ , fits the data excellently. *This is our main result.*

The parameters  $a$  and  $b$  in (52) have been determined by finding the visually best straight line for each data set. These best lines are shown in the figures. The quality of the fits vary. The data in figure 1 fit the best to a straight line, whereas the data that fit to a straight line the least are found in figure 5. This is reflected in the uncertainty of the coefficients  $a$  and  $b$ . The uncertainty is in general larger in  $a$  than in  $b$ . Note that the  $a$  and  $b$  coefficients for drainage and imbibition in figure 2 and 3 are slightly different.

In the first two columns of figures 1 — 7 where we have plotted  $v_p$  and  $v_m$  against  $S_w$ , we have fitted the data to polynomials; for  $v_p$  we have used fourth order polynomials for the numerical fits and for  $v_m$  we have used third order polynomials. The reason for this lies in equation (52) which indicates that  $v_m$  should be modeled with a polynomial of one less order than that of  $v_p$ . The  $v_p$ -polynomial is numerically fitted directly to the data. For the  $v_m$  fit, one can either I: fit a third order polynomial directly to the data, or II: calculate the coefficients for the  $v_m$  fit using those found for  $v_p$  using equation (52). In principle, these two methods should give the same results. However, method II is highly sensitive to noise in the data series. Method II was used for all the data set, and the correspondence is good between the fit and the data for the sets with the lowest amount of deviation, figure 1 in particular. Here, method II showed only small deviations from method I in the initial and final values of the data series. Method I was used in all of the plots, as the method of fit for  $v_p$  and  $v_m$  does not affect the rest of the results.

We plot in figure 8 the values of the coefficients  $a$  and  $b$  as a function of the pressure gradient for all the data series. The pressure  $\Delta P$  is rendered dimensionless by dividing it by  $\mu_w v_0 / K$ ,  $\Delta P_\lambda = \Delta P K / \mu_w v_0$ .

#### 4. The average seepage velocity $v_p$ and the co-Moving velocity $v_m$ in a dynamic pore network model

The porous medium is represented by a network of nodes and links in dynamic pore network modeling [38]. The immiscible fluids are transported through the links which are connected at the nodes. The dynamic pore network model we consider here was introduced by Aker et al. [39]. A recent review describe it in detail, see [42].

The nodes do not contain fluid, only the links do. The nodes only represent the points where the links meet. The flow rate  $q_j$  inside any link  $j$  of the network at any instant of time is obtained by [31, 56],

$$q_j = -\frac{g_j}{l_j \mu_{av}} [\Delta p_j - \sum p_{c,j}], \quad (53)$$

where  $l_j$  is the link length,  $g_j$  is the link permeability which depends on the cross section of the link and  $\Delta p_j$  is the pressure drop across link. The viscosity term  $\mu_{av}$  is the saturation-weighted viscosity of the fluids inside the link given by  $\mu_{av} = s_{j,w} \mu_w + s_{j,n} \mu_n$  where  $s_{j,w}$  and  $s_{j,n}$  are the wetting and non-wetting fluid saturations inside the link. The term  $\sum p_{c,j}$  is the total interfacial pressure from the fluid interfaces in the link  $j$ . A pore typically consists of two wider pore bodies connected by a narrow pore throat. We model this by using hour-glass shaped links. The variation of the interfacial pressure with the

interface position for such a link is modeled by [31]

$$|p_c(x)| = \frac{2\gamma\cos\theta}{r_j} \left[ 1 - \cos\left(\frac{2\pi x}{l_j}\right) \right], \quad (54)$$

where  $r_j$  is the average radius of the link and  $x \in [0, l_j]$  is the position of the interface inside the link. Here,  $\theta$  is the contact angle between the interface and the pore wall and  $\gamma$  is the surface tension between the fluids.

These two equations (54) and (53), together with the Kirchhoff relations, i.e., the sum of the net volume flux at every node at each time step will be zero, provide a set of linear equations. In order to calculate the local flow rates, we solve these equations with a conjugate gradient solver [57]. All the interfaces are then advanced accordingly using small time steps.

In order to achieve steady-state flow, we apply periodic boundary conditions in the direction of flow.

We use a two-dimensional square lattice with  $64 \times 64$  links with link lengths  $l_j = 1$  mm. Disorder is introduced by choosing the link radii  $r_j$  randomly from a uniform distribution in the range 0.1 mm to 0.4 mm. We use 100 different realizations of such networks for our simulations.

Assuming Poiseuille flow in the links, the average link permeability  $r_j^2/8$  will be  $7.8 \times 10^{-7} \text{ m}^2$ . As it is a square lattice, the length of it compensates for its width, making its permeability equal to the link permeability times  $\sqrt{2}$  to account for its  $45^\circ$  tilt. This gives an estimate for the average permeability of the lattice around  $5.5 \times 10^{-7} \text{ m}^2$ .

We will in the following explore  $v_p$  and  $v_m$  as a function of the wetting saturation  $S_w$  defined as the total volume of wetting fluid in the links divided by their total pore volume, and the average pressure gradient defined as  $\Delta P/L$  where  $\Delta P$  is the pressure difference across the network. The viscosity ratio  $M$  is defined as the ratio of the viscosity  $\mu_n$  of non-wetting fluid to the viscosity  $\mu_w$  of the wetting fluid ( $M = \mu_n/\mu_w$ ).

#### 4.1. Fitting the average seepage velocity $v_p$ and the co-moving velocity $v_m$ to polynomials

We discuss here  $v_p$  and  $v_m$  as a function of the wetting saturation  $S_w$  for fixed pressure gradient  $\Delta P/L$ . The average seepage velocity  $v_p$  is measured directly from the model. The co-moving velocity is inferred from the velocity difference  $v_n - v_w$  and the derivative  $dv_p/dS_w$  according to equation (25). We fit the data to the polynomials

$$v_p = \sum_{k=0}^4 C_k S_w^k, \quad (55)$$

and

$$v_m = \sum_{k=0}^3 D_k S_w^k. \quad (56)$$

We find that the three or fourth order polynomials form an adequate compromise between accuracy and the wish to keep the number of fitting parameters down.

Figure 9 shows how the seepage velocity  $v_p$  behaves as a function of the wetting saturation  $S_w$  for four different pressure gradients:  $\Delta P/L = 0.22, 0.5, 0.71$  and  $1.0$  MPa/m. The results are obtained for  $0.05 \leq S_w \leq 0.95$  with intervals of 0.05, totaling 20 data points. For now, we use  $\mu_w = 0.03$  Pa s and  $\mu_n = 0.01$  Pa s, i.e.,  $M = \mu_n/\mu_w = 1/3$ . The effect of a varying viscosity ratio will be explored later in this paper. We observe the quality of the fits to improve with increasing pressure gradient.

We use the data in figure 9 to approximate  $v'_p$  by central differencing, which then is used to determine  $v_m$  from equation (25). We show the result in figures 9 where we plot  $v_m$  as a function of  $S_w$ .

We plot  $v_m$  against  $v'_p$  in figure 11 for fixed  $\Delta P/L = 0.22, 0.50, 0.71, 1.0, 1.4$  and  $2.1$  MPa/m. We introduce a velocity scale  $v_0 = v_p(S_w = 1, \Delta P/L)$  to make the fits comparable to the relative permeability-based fits we discussed in Section 3. As is evident, equation (52) fits the data well. We note that both  $a$  and  $b$  vary with the pressure gradient  $\Delta P/L$ . Hence, we write equation (52) as

$$v_m\left(S_w, \frac{\Delta P}{L}\right) = a\left(\frac{\Delta P}{L}\right) v_0\left(\frac{\Delta P}{L}\right) + b\left(\frac{\Delta P}{L}\right) \frac{dv_p}{dS_w}\left(S_w, \frac{\Delta P}{L}\right). \quad (57)$$

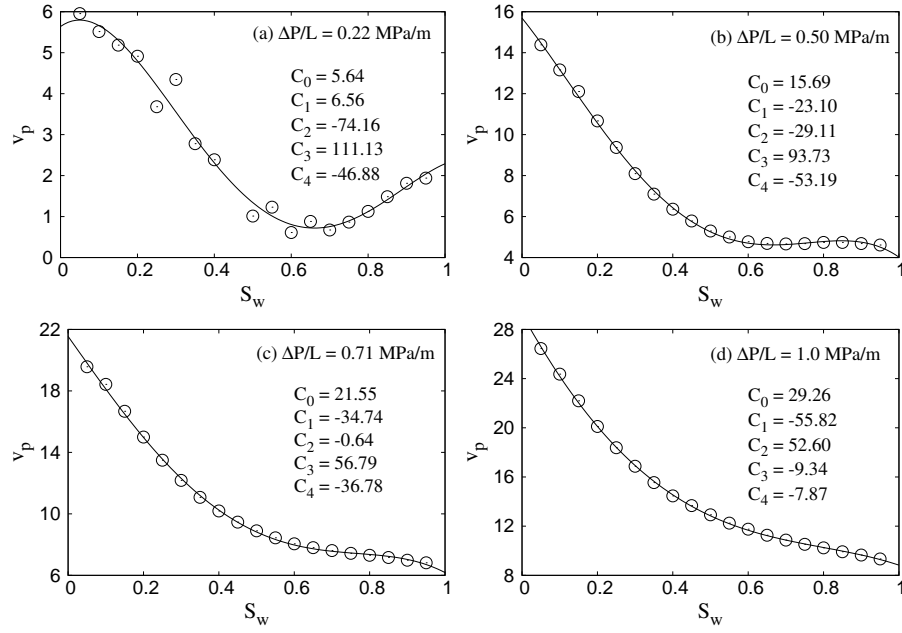


Figure 9: Fitting of the numerical results for  $v_p$  vs  $S_w$  with equation (55) with  $\mu_w = 0.03$  Pa s and  $\mu_n = 0.01$  Pa s (i.e.,  $M = 1/3$ ), and for four different pressure gradients,  $\Delta P/L = 0.22, 0.50, 0.71$  and  $1.0$  MPa/m. The fitting parameters are shown in the legends in each figure. The rate of change of  $v_p$  ( $v'_p = dv_p/dS_w$ ) will be calculated from this figure and will be used to express  $v_m$  in terms of  $v'_p$  in figure 10.

We have in this equation written explicitly what parameters each variable depends upon. This will become important in the next section.

#### 4.2. The co-moving velocity when $dv_p/dS_w$ is treated as an independent variable

The co-moving velocity  $v_m$  has been calculated using the dynamic network model in both References [22] and [42]. In contrast to our approach here, the derivative  $v'_p$  was treated as an independent variable in those papers. That is,  $v_m$  was plotted against  $(S_w, v'_p)$  producing a plane. In [22], a variant of the dynamic pore network model we use here was used [40], resulting in the relation

$$v_m \left( S_w, \frac{dv_p}{dS_w} \right) = c + d S_w + e \frac{dv_p}{dS_w}, \quad (58)$$

where  $c \approx -0.095$ ,  $d \approx -0.15$  and  $e \approx 0.79$  for data averaged over both square and hexagonal lattices. Sinha et al. considered both a square lattice and a lattice based on a reconstructed Berea sandstone, giving  $c = 5.00 \pm 0.13$ ,  $d = -6.36 \pm 0.25$  and  $e = 0.94 \pm 0.01$  for the square lattice and  $c = 10.10 \pm 0.32$ ,  $d = -12.94 \pm 0.62$  and  $e = 0.88 \pm 0.01$  for the reconstructed Berea sandstone.

Equation (57) constitutes a cut through the plane  $(S_w, v'_p)$  given by  $\Delta P/L$  constant. It is an open question as to why the explicit  $S_w$  dependence disappears in equation (57) when making this cut.

#### 4.3. Dependence of coefficients $a$ and $b$ on the pressure gradient

Figure 12 shows the variation of  $av_0$  and  $b$  defined in equation (57), as a function of the pressure gradient  $\Delta P/L$ . We observe two different regions as the fluid velocities increase with increasing pressure gradient. We name these regions I and II.

*Region I* — This is the low pressure gradient region. We find a good fit to the data with the line  $av_0 = 0.7m/s - 1.1(\Delta P/L)m^2/MPa.s$ . The coefficient  $b$  has a value around 0.76. Due to low flow velocity, the  $av_0$  and  $b$  found in this region can be compared with the relative permeability data in Section 3.

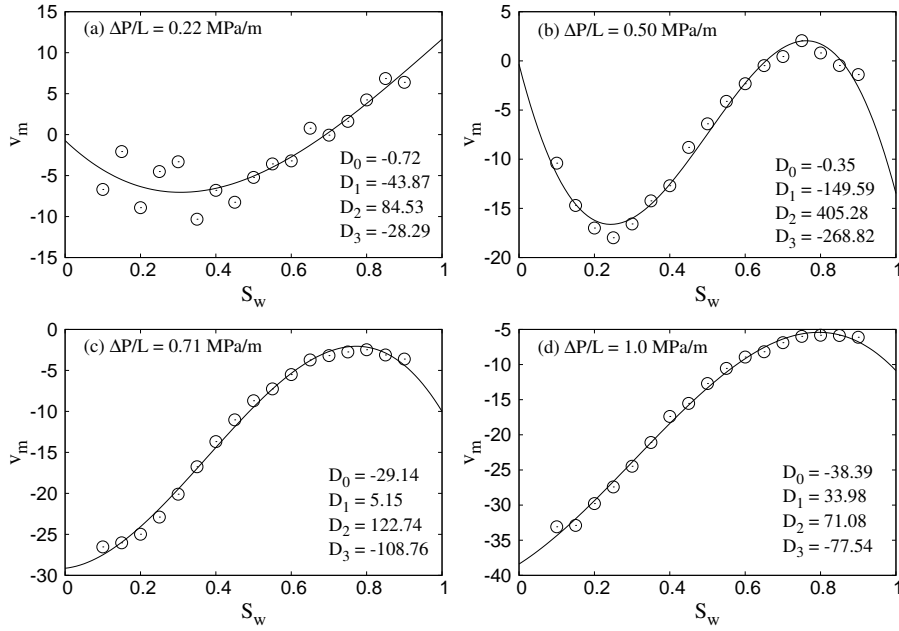


Figure 10: Fitting of the numerical results for  $v_m$  vs.  $S_w$  using equation (56). The parameters  $M$  and  $\Delta P/L$  are as in Figure 9.

*Region II* — This is the high pressure gradient region. Here  $av_0$  saturates to a value near  $-0.1$  m/s whereas  $b$  approaches the value 1 asymptotically. This is outside the region where the relative permeability data would be relevant.

The crossover of  $av_0$  from positive to negative value and the onset of increment in  $b$  is observed to take place around the same pressure gradient.

#### 4.4. $v_p$ as a function of $S_w$ and $\Delta P/L$

We now turn to the average seepage velocity  $v_p$ . As described in the Introduction, there is a regime over an interval of pressure gradients where the flow rate is proportional to the pressure gradient to a power [24–29]. This regime is clearly visible in our dynamic pore network model [30, 37]. Our aim in this section is to map out the  $v_p$  over a wide range of saturations  $S_w$  and pressure gradients  $\Delta P/L$ .

Figure 13(a) shows how the flow rate  $Q$  increases as the pressure gradient  $\Delta P/L$  increases. We observe the following behavior:

$$Q \propto \begin{cases} 0 & , |\Delta P| \leq P_s , \\ \left( \left| \frac{\Delta P}{L} \right| - \frac{P_s}{L} \right)^\beta & , |\Delta P| > P_s , \end{cases} \quad (59)$$

where  $P_s$  is a threshold pressure below which there is no flow. This threshold is a finite-size effect, see [35]. Above a pressure difference  $|\Delta P| \gg P_t$ , the exponent  $\beta = 1$  and we observe Darcy-like linear flow. Below this pressure difference,  $P_s < |\Delta P| < P_t$ , the exponent  $\beta > 1$ .

The inset in figure 13(a) demonstrates how the threshold pressure  $P_s$  and  $\beta$  were calculated: For a constant  $S_w$ , we first set a particular  $\beta$  value and fit the numerical results to equation (59), finding  $P_s$  as well as the error associated with the fit. In this way we get a  $P_s$  value and an error value as a function of  $\beta$ . The curves in the inset show the error as a function of  $\beta$  for different saturations. We identify the minimum of the error vs.  $\beta$  curve. The value of  $\beta$  giving the error minimum and the corresponding  $P_s$  value are the values we assign to the system for that saturation  $S_w$ .

Figures 13(b) and (c) show the variation of exponent  $\beta$  and the transition point  $P_t$  as functions of the wetting saturation  $S_w$ . Both  $\beta$  and  $P_t$  is observed to have a maximum at  $S_w = 0.5$  to decrease on both sides of it. We have that  $\beta = 1$  for  $S_w = 0$  and  $S_w = 1$  as we are then dealing with single fluid flow.

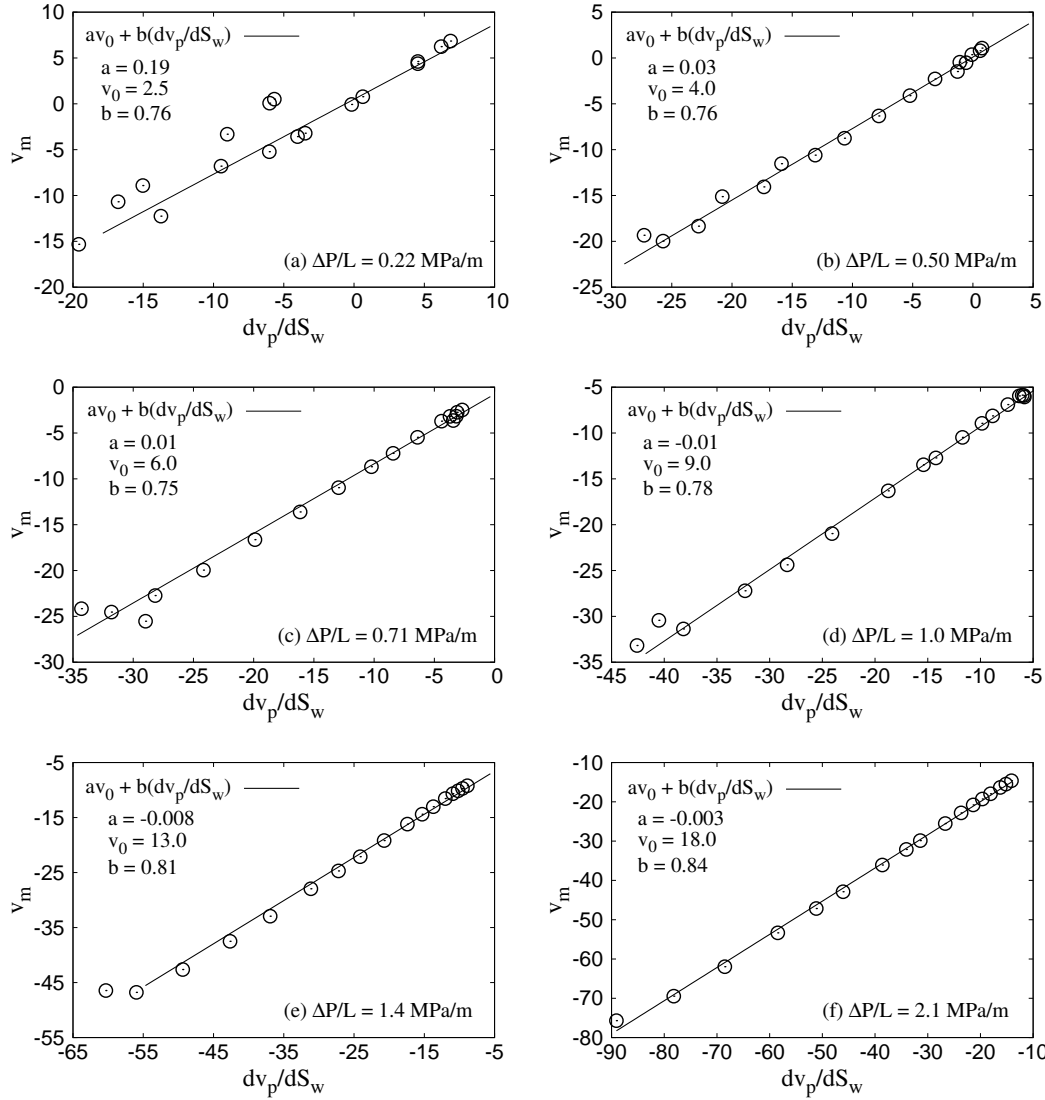


Figure 11: The co-moving velocity as a function of  $dv_p/dS_w$  from equation (25) for  $\mu_w = 0.03$  Pa s and  $\mu_n = 0.01$  Pa s, and  $\Delta P/L = 0.22, 0.5, 0.71, 1.0, 1.4$  and  $2.1$  MPa/m.

Figure 14 shows the flow rate  $Q = v_p A_p$  (equation (10)) as a function of the wetting saturation  $S_w$  for four different pressure gradients,  $\Delta P/L = 0.22, 0.40, 0.50$  and  $0.71$  MPa/m. The data points shown as red squares indicate that the flow is in the non-linear regime where  $\beta > 1$ , i.e.,  $P_s < |\Delta P| < P_t$ . The data points shown as blue circles indicate that the flow is in the linear regime, i.e.,  $|\Delta P| > P_t$ . Hence, we see that for a range of pressure gradients, e.g.,  $\Delta P/L = 0.4$  MPa/m,  $v_p$  visits both the linear and non-linear regimes over the range of wetting saturations  $S_w$ . For pressure gradients larger than  $0.5$  MPa/m,  $v_p$  is always in the linear regime over the entire range of  $S_w$ .

We now compare figures 13 and 14. We note that the transition between the linear and non-linear regimes in figure 14 appears at essentially the same pressure gradient that separates regimes I and II in figure 13. This points towards a connection. However, such a connection is yet to be found.

#### 4.5. Limits

The irreducible wetting saturation  $S_{w,irr}$  is the minimum wetting saturation possible irrespective of the pressure gradient. The residual non-wetting saturation  $S_{n,r}$  is the minimum non-wetting saturation possible irrespective of the pressure gradient. At any finite pressure gradient  $\Delta P/L$  there will be a minimum wetting saturation  $S_{w,min}(\Delta P/L)$  which approaches  $S_{w,irr}$  as

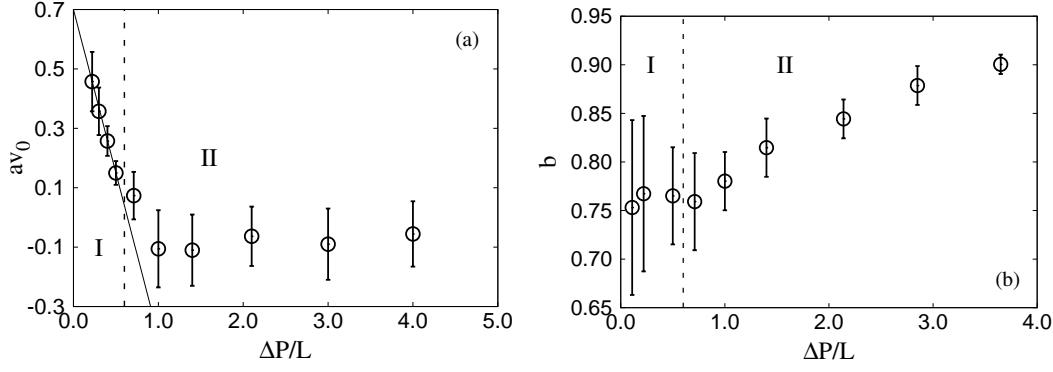


Figure 12: (a) and (b) respectively shows  $av_0$  and  $b$  defined in equation (57) as a function of the pressure gradient  $\Delta P/L$ . The viscosities of the fluids were  $\mu_w = 0.03$  Pa s and  $\mu_n = 0.01$  Pa s, so that  $M = 1/3$ . We have marked two regions, I and II in both (a) and (b). The straight line in region I in (a) is  $0.7m/s - 1.1(\Delta P/L)m^2/MPas$ .

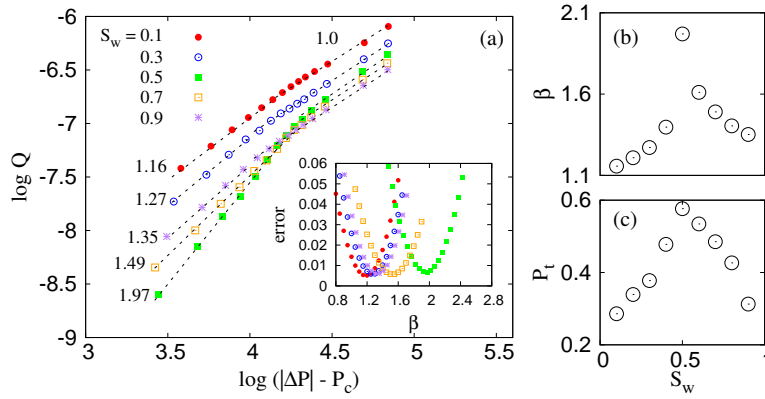


Figure 13: (a) shows  $Q$  vs.  $\Delta P$  for wetting saturations  $S_w = 0.1, 0.3, 0.5, 0.7$  and  $0.9$ . The viscosities of the fluids were  $\mu_w = 0.03$  Pa s and  $\mu_n = 0.01$  Pa s. The inset shows the fitting error between the data and equation (59) as a function of  $\beta$  for the different wetting saturations. (b) and (c) show the dependence of  $P_t$  and  $\beta$  on  $S_w$ .

the pressure gradient is increased. Likewise, there will be for any finite pressure gradient a minimum non-wetting saturation  $S_{n,\min}(\Delta P/L)$  which approaches  $S_{n,r}$  as the pressure gradient is increased. Let us define  $S_{w,\max}(\Delta P/L) = 1 - S_{n,\min}(\Delta P/L)$ . When  $S_w$  reaches  $S_{w,\min}(\Delta P/L)$  or  $S_{w,\max}(\Delta P/L)$ , either the wetting or the non-wetting fluid stops moving.

Knudsen and Hansen [43] demonstrated that there is hysteresis at  $S_{w,\min}(\Delta P/L)$  based on a dynamic pore network model closely related to the one we use here, see their Figure 2. The way Knudsen and Hansen did this was to increase or decrease the saturation step by step, building on the steady-state configurations that already were established at the previous saturation.

In the numerical work we present here based on the dynamic pore network model, we re-initiate the model every time we change the saturation. This means that the system for each value of the saturation chooses the most stable branch, masking the hysteresis. It is in this spirit we present our results in the following.

Using equation (10), we have that either

$$v_p = v_n(1 - S_w), \quad \text{for } S_w \rightarrow (S_{w,\min})^+, \quad (60)$$

or

$$v_p = v_w S_w \quad \text{for } S_w \rightarrow (S_{w,\max})^-, \quad (61)$$

Hence, we have

$$\frac{dv_p}{dS_w} = -v_n \quad \text{for } S_w \rightarrow (S_{w,\min})^+, \quad (62)$$

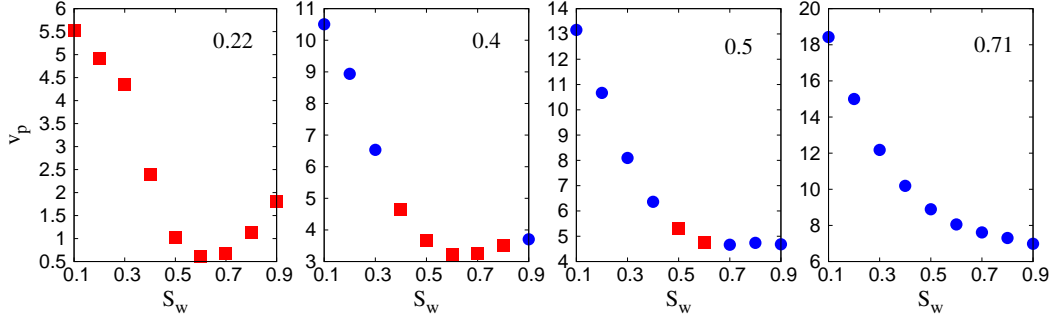


Figure 14:  $v_p$  as a function of saturation  $S_w$  for  $\Delta P/L = 0.22, 0.40, 0.50$  and  $0.71$  MPa/m respectively. The viscosities of the fluids were  $\mu_w = 0.03$  Pa s and  $\mu_n = 0.01$  Pa s. A red square indicates that the flow is in the non-linear region for the set of parameters,  $\Delta P/L$  and  $S_w$ , that produce this data point. A blue circle indicates that the flow is in the linear region.

or

$$\frac{dv_p}{dS_w} = v_w \quad \text{for } S_w \rightarrow (S_{w,\max})^-, \quad (63)$$

Combining these two equations with equation (25), we find that

$$v_m = 0 \quad \text{for } S_w \rightarrow (S_{w,\min})^+ \text{ or } S_w \rightarrow (S_{w,\max})^-. \quad (64)$$

We show in figure 15(a) and (b) the wetting and non-wetting seepage velocities as a function of  $S_w$  for pressure gradients  $\Delta P/L = 0.22, 0.30, 0.40$  and  $0.50$  MPa/m. The viscosities were  $\mu_w = 0.03$  Pa s and  $\mu_n = 0.01$  Pa s. Both of the seepage velocities  $v_w$  and  $v_n$  signal a non-zero  $S_{w,\min}(\Delta P/L)$ . However, we find that  $S_{w,\max}(\Delta P/L) = 1$ .

We denote  $v_n = v_n^*$  the non-wetting seepage velocity we find for  $S_w < S_{w,\min}(\Delta P/L)$ . It is possible to reach such saturations by initiating the network with a saturation  $S_w$  and a pressure difference  $\Delta P_i/L$  making  $S_w > S_{w,\min}(\Delta P_i/L)$ , and then reduce the pressure difference to  $\Delta P/L$  such that  $S_w < S_{w,\min}(\Delta P/L)$ .

We show in figure 15(c)  $v_p/v_n$  as a function of  $S_w$ . The straight line is the function  $1 - S_w$ . By comparing with figure 15(b) that as soon as  $S_w < S_{w,\min}(\Delta P/L)$ , the data for  $v_p/v_n$  follows the line  $1 - S_w$ . This is in accordance with equation (60).

This teaches us the following: For  $v_p = (1 - S_w)v_n^*$ , i.e., when  $S_w < S_{w,\min}(\Delta P/L)$ , we have  $dv_p/dS_w = -v_n^*$  and  $v_m = 0$ , see equation (64). If we now compare with figure 11, we see that the fits to equation (57) do not pass through this point,  $(dv_p/dS_w, v_m) = (-v_n^*, 0)$ . The difference is too large to be attributed to the uncertainty of the fits. We note that we are here dealing with single phase flow. If the constitutive law for  $v_m$  in equation (57) is the result of correlations appearing in two-phase flow, there is no reason for the single fluid case to fall on this curve.

We will in the future present an full analysis of this problem, taking hysteresis fully into account.

We now turn to the limit where the capillary number is so high that the capillary forces are negligible compared to the viscous forces. We achieve this limit in the dynamic pore network model by setting the surface tension  $\gamma$  in equation (54) to zero. If the viscosities of the two fluids are equal, there will be no difference between the fluids and  $v_w = v_n$ . Furthermore, we will have that  $v_p$  is independent of the wetting saturation  $S_w$ , so that  $dv_p/dS_w = 0$ . From equation (25) we then have that the co-moving velocity  $v_m = 0$ .

We show in figure 16,  $v_m$  as a function of  $dv_p/dS_w$  in the limit of  $\gamma = 0$  but with the fluid viscosities being  $\mu_w = 0.03$  Pa s and  $\mu_n = 0.01$  Pa s respectively. We find that  $v_m$  follows equation (57) with  $av_0 = -0.06$  and  $b = 0.99$ . From equations (10), (23) and (24), we then have that  $v_n = v_w = v_p$ .

#### 4.6. Viscosity ratio $M$

We will here discuss how the viscosity of the two fluids will affect the relation between  $v_p$  and  $v_m$ . We will also discuss how the parameters  $av_0$  and  $b$  depend on the fluid viscosities  $\mu_w$  and  $\mu_n$ .



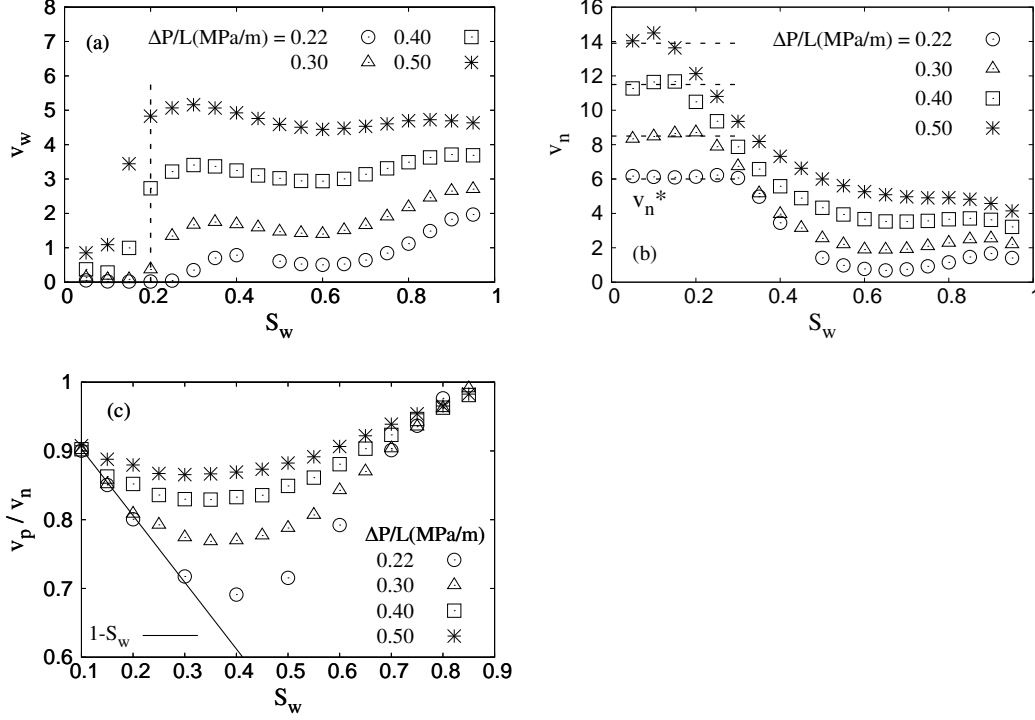


Figure 15: (a)  $v_w$  as a function of the wetting saturation  $S_w$  for  $\Delta P = 0.22, 0.30, 0.40$  and  $0.50$  MPa/m. The vertical dotted line shows the value of  $S_{w,\min}(\Delta P)$  below which  $v_w \approx 0$ . (b)  $v_n$  as a function of the wetting saturation  $S_w$ . The horizontal dotted lines show  $v_n^*$  when  $S_w < S_{w,\min}$ . (c) shows the comparison of the numerical results with equation (60) (see the dotted line) for all 4 pressure gradients. The viscosities of the fluids were  $\mu_w = 0.03$  Pa s and  $\mu_n = 0.01$  Pa s.

Figure 17 shows how co-moving velocity behaves as a function of  $dv_p/dS_w(S_w, \Delta P/L)$  for different values of saturation, see equation (57) when the fluid viscosities are changed. We compare  $v_m$  as a function of  $dv_p/dS_w$  for viscosity ratio  $M = 3$  ( $\mu_w = 0.03$  Pa s and  $\mu_n = 0.01$  Pa s) with viscosity ratio  $M = 1/3$  ( $\mu_w = 0.01$  Pa s and  $\mu_n = 0.03$  Pa s). Figures 17(a), (b), (c) and (d) respectively are based on pressure gradients  $\Delta P/L = 0.22, 0.5, 1.0$  and  $1.4$  MPa/m. We find that both coefficients  $av_0$  and  $b$  change considerably when the viscosity ratio is inverted. For both  $M$  values, the co-moving velocity follows equation (57). For  $M = 1/3$ ,  $av_0$  decreases with increasing pressure gradient. The coefficient  $b$  remains at value around 0.76 until the pressure gradient exceeds a value around  $\Delta P/L > 0.5$  MPa/m. On the other hand, for  $M = 3$ ,  $av_0$  and  $b$  remain constant around 1.5 and 0.94 respectively irrespective of the pressure gradients we have considered.

We plot in figure 18 the coefficients  $av_0$  and  $b$  as functions of the viscosity ratio  $M$  for different values of the pressure gradient  $\Delta P/L$ . For the chosen span of parameters, we observe three distinct regions:

**Region A** ( $M \leq 1$ ) - In this region, both  $av_0$  and  $b$  seem independent of  $M$ . Moreover,  $b$  remains constant around 0.77 for  $\Delta P/L < 0.5$  MPa/m and increases for larger values of the pressure gradient.  $av_0$  decreases with increasing pressure gradient as long as  $\Delta P/L < 0.5$  MPa/m. Beyond this limit,  $av_0$  saturates at a value close to zero.

**Region B** ( $1 \leq M \leq 2$ ) - In this region  $av_0$  and  $b$  are both increasing functions of  $M$ .

**Region C** ( $M \geq 2$ ) - In this region,  $av_0$  and  $b$  neither changes with viscosity ratio  $M$  nor with the pressure gradient  $\Delta P/L$ .

## 5. Discussion

The aim of this paper has been to expand on the theory based on Euler homogeneity that was first presented in [22]. It provides a number of relations between the seepage velocities of each fluid involved which together with constitutive equations for the average fluid velocity and the co-moving velocity form a closed set of equations.

It has recently been discovered that the constitutive equation for the average seepage velocity of the fluids follows a power law in the pressure gradient for a range of parameter values [24–29]. Relative permeability theory offers the mapping

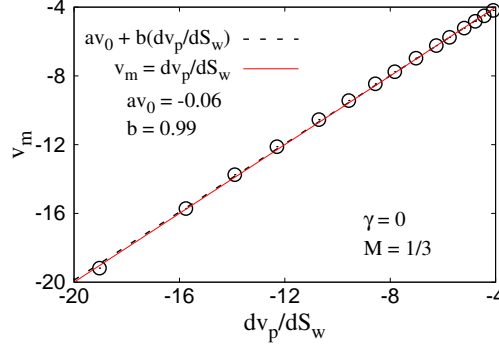


Figure 16: The figure shows how  $v_m$  varies with  $v_p' (= dv_p/dS_w)$  in the limit of large capillary numbers when the capillary forces are vanishingly small compared to the viscous forces. We have set the surface tension  $\gamma = 0$  in the dynamic pore network model, while keeping  $\mu_w = 0.03$  Pa s and  $\mu_n = 0.01$  Pa s. For reference, the red solid line represents the equation:  $v_m = dv_p/dS_w$ .

$(v_w, v_n) \rightarrow v_p$ . However, the non-linear constitutive equation for  $v_p$  requires the opposite mapping  $v_p \rightarrow (v_w, v_n)$ , which is indeterminate within relative permeability theory. Euler homogeneity theory, on the other hand, offers the two-way mapping  $(v_w, v_n) \Leftrightarrow (v_p, v_m)$ , which is readily combined with the non-linear constitutive equation for  $v_p$ . It is an additional bonus that the constitutive equation for  $v_m$ , equation (52), is as simple as it is.

The co-moving velocity which together with the average seepage velocity of the fluids closes the equation set as described in Section 2.3, is related to the seepage velocity difference  $v_n - v_w$ , but it is not the same, see equations (25) and (26). We discuss in Section 2.4 the interpretation of  $v_m$ . It should be noted that the co-moving velocity is not associated volume transport, see equation (40).

We determine the constitutive equation for the co-moving velocity from relative permeability data found in the literature in Section 3. We do this by *reverse engineer* the data which have been cast in the form of relative permeability curves.

Our main result is equation (52), which shows that the co-moving velocity is linear in the derivative of the average seepage velocity with respect to the saturation when the pressure gradient is kept fixed, see figures 1 to 7. It is an open question as to why this is so.

Since we do not have theory as to why the co-moving velocity takes the simple form it does, we have not applied any particular criterion for which data sets to investigate. Any attempt at this would taint the results by our preconception on what causes the functional form (52). In particular, we have not taken the possibility for hysteresis into account. We discuss why it is still permissible to treat hysteretic data as representatives of analytic functions in Subsection 2.1.

We continue in Section 4 to consider the constitutive equation for the co-moving velocity. We find the same constitutive equation as in equation (52), see figure 11. It is remarkable that this remains true also when the constitutive equation for the average seepage velocity moves into the power-law region, see Section 4.4.

We have in this paper only considered systems without a saturation gradient. This has allowed us to ignore capillary pressure effects. A next step is to incorporate such a saturation gradient into the system to observe how the constitutive equation (52) for the co-moving velocity changes.

## 6. Acknowledgment

This work was partly supported by the Research Council of Norway through its Centres of Excellence funding scheme, project number 262644. SS was supported by the National Natural Science Foundation of China under grant number 11750110430. We thank D. Bedeaux, C. F. Berg, H. Cheon, H. Fyhn, M. Aa. Gjennestad, S. Kjelstrup and P. A. Slotte for discussions.

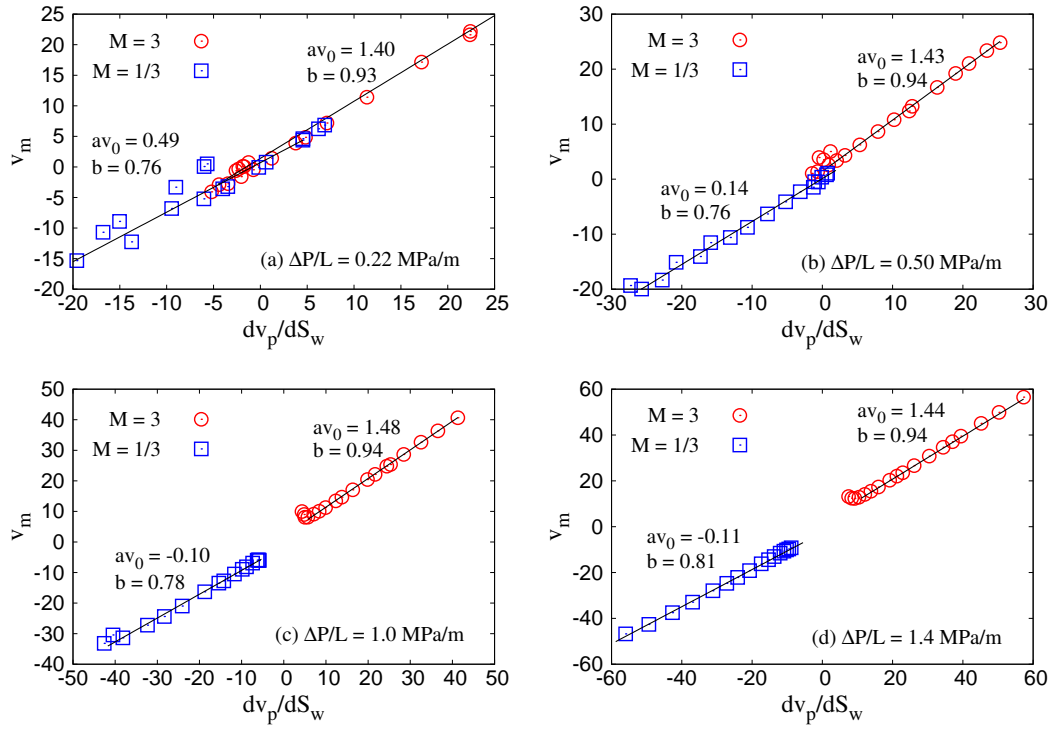


Figure 17: Variation of  $v_m$  with  $dv_p/dS_w$  for four different pressure gradient: (a) 0.22, (b) 0.50, (c) 1.0 and (d) 1.4 MPa/m. Results are shown for two different viscosity ratios:  $M = 3$  ( $\mu_w = 0.03$  Pa s and  $\mu_n = 0.01$  Pa s) shown as blue squares and  $M = 1/3$  ( $\mu_w = 0.01$  Pa s and  $\mu_n = 0.03$  Pa s) as red circles.

## References

- [1] J. Bear, Dynamics of Fluids in Porous Media (Dover, Mineola, 1988).
- [2] M. J. Blunt, Multiphase Flow in Permeable Media (Cambridge University Press, Cambridge, 2017).
- [3] R. D. Wyckoff and H. G. Botset, The Flow of Gas-Liquid Mixtures Through Unconsolidated Sands, *Physics* **7**, 325-345 (1936); doi.org/10.1063/1.1745402.
- [4] M. C. Leverett, Capillary Behavior in Porous Sands, *Trans. AIMME*, **12**, 152 (1940).
- [5] S. M. Hassanizadeh and W. G. Gray, Mechanics and Thermodynamics of Multiphase Flow in Porous Media Including Interphase Boundaries, *Adv. Water Res.* **13**, 169 (1990); 10.1016/0309-1708(90)90040-B.
- [6] S. M. Hassanizadeh and W. G. Gray, Towards an Improved Description of the Physics of Two-Phase Flow, *Adv. Water Res.* **16**, 53 (1993); doi.org/10.1016/0309-1708(93)90029-F.
- [7] S. M. Hassanizadeh and W. G. Gray, Thermodynamic Basis of Capillary Pressure in Porous Media, *Water Resour. Res.* **29**, 3389 (1993); doi.org/10.1029/93WR01495.
- [8] J. Niessner, S. Berg and S. M. Hassanizadeh, Comparison of Two-Phase Darcy's Law with a Thermodynamically Consistent Approach, *Transp. Por. Med.* **88**, 133 (2011); doi.org/10.1007/s11242-011-9730-0.
- [9] W. G. Gray and C. T. Miller, Introduction to the Thermodynamically Constrained Averaging Theory for Porous Medium Systems, (Springer Verlag, Berlin, 2014).
- [10] S. Whitaker, Flow in Porous Media II: The Governing Equations for Immiscible, Two-Phase Flow, *Transp. Por. Med.* **1**, 105 (1986); doi:10.1007/BF00714688.

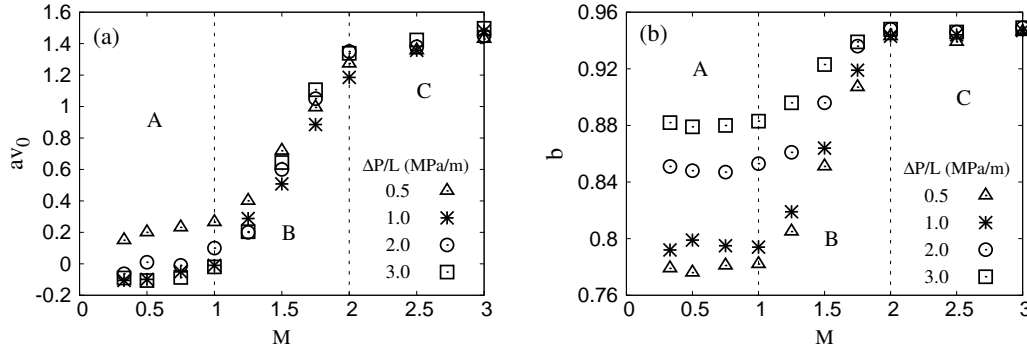


Figure 18: Variation of  $aV_0$  and  $b$  with viscosity ratio  $M$  for a constant pressure gradient  $\Delta P/L$ . The numerical results are repeated for four different pressure gradients,  $\Delta P/L = 0.5, 1.0, 2.0$  and  $3.0$  MPa/m. For  $M = 1.0$ , we set  $\mu_n = 0.01$  Pa s and  $\mu_w = 0.01$  Pa s. For  $M > 1$ , we keep  $\mu_w = 0.01$  Pa s while  $\mu_n$  has a value  $M\mu_w$  Pa s. On the other hand, for  $M < 1$ , we keep  $\mu_n = 0.01$  Pa s while  $\mu_w$  has a value  $\mu_n/M$  Pa s.

- [11] S. Kjelstrup, D. Bedeaux, A. Hansen, B. Hafskjold and O. Galteland, Non-Isothermal Transport of Multi-Phase Fluids in Porous Media. The entropy production , *Front. Phys.* **6**, 126 (2018); doi.org/10.3389/fphy.2018.00126.
- [12] S. Kjelstrup, D. Bedeaux, A. Hansen, B. Hafskjold and O. Galteland, Non-Isothermal Transport of Multi-Phase Fluids in Porous Media. Constitutive equations, *Front. Phys.* **6**, 150 (2019); doi.org/10.3389/fphy.2018.00150.
- [13] R. Hilfer and H. Besserer, Macroscopic two-phase flow in porous media , *Physica B*, **279**, 125 (2000); doi.org/10.1016/S0921-4526(99)00694-8.
- [14] R. Hilfer, Capillary pressure, hysteresis and residual saturation in porous media , *Physica A*, **359**, 119 (2006); doi.org/10.1016/j.physa.2005.05.086.
- [15] R. Hilfer, Macroscopic capillarity and hysteresis for flow in porous media , *Phys. Rev. E*, **73**, 016307 (2006); doi.org/10.1103/PhysRevE.73.016307.
- [16] R. Hilfer, Macroscopic capillarity without a constitutive capillary pressure function , *Physica A*, **371**, 209 (2006); doi.org/10.1016/j.physa.2006.04.051.
- [17] R. Hilfer and F. Döster, Percolation as a basic concept for capillarity , *Transp. Por. Med.* **82**, 507 (2010); doi.org/10.1007/s11242-009-9395-0.
- [18] F. Döster, O. Hönig and R. Hilfer, Horizontal Flow and Capillarity-Driven Redistribution in Porous Media , *Phys. Rev. E*, **86**, 016317 (2012); doi.org/10.1103/PhysRevE.86.016317.
- [19] M. S. Valavanides, G. N. Constantinides and A. C. Payatakes, Mechanistic Model of Steady-State Two-Phase Flow in Porous Media Based on Ganglion Dynamics , *Transp. Porous Media* **30**, 267-299 (1998); doi.org/10.1023/A:1006558121674.
- [20] M. S. Valavanides, Steady-State Two-Phase Flow in Porous Media: Review of Progress in the Development of the DeProF Theory Bridging Pore- to Statistical Thermodynamics-Scales , *Oil Gas Sci. Technol.* **67**, 787-96804 (2012); doi.org/10.2516/ogst/2012056.
- [21] M. S. Valavanides, Review of Steady-State Two-Phase Flow in Porous Media: Independent Variables, Universal Energy Efficiency Map, Critical Flow Conditions, Effective Characterization of Flow and Pore Network , *Transp. Porous Media*, **123**, 45–99 (2018); doi.org/10.1007/s11242-018-1026-1.

- [22] A. Hansen, S. Sinha, D. Bedeaux, S. Kjelstrup, M. A. Gjennestad and M. Vassvik, Relations Between Seepage Velocities in Immiscible, Incompressible Two-Phase Flow in Porous Media , *Transp. Porous Media* **125**, 565 (2018); doi:10.1007/s11242-018-1139-6.
- [23] S. Roy, S. Sinha and A. Hansen, Flow-area relations in immiscible two-phase flow in porous media, *Front. Phys.* **8**, 4 (2020); doi.org/10.3389/fphy.2020.00004.
- [24] K. T. Tallakstad, H. A. Knudsen, T. Ramstad, G. Løvoll, K. J. Måløy, R. Toussaint and E. G. Flekkøy, Steady-State Two-Phase Flow in Porous Media: Statistics and Transport Properties , *Phys. Rev. Lett.* **102**, 074502 (2009); doi: 10.1103/PhysRevLett.102.074502.
- [25] K. T. Tallakstad, G. Løvoll, H. A. Knudsen, T. Ramstad, E. G. Flekkøy and K. J. Måløy, Steady-State Simultaneous Two-Phase Flow in Porous Media: an Experimental Study , *Phys. Rev. E* **80**, 036308 (2009); doi.org/10.1103/PhysRevE.80.036308.
- [26] O. Aursjø, M. Erpelding, K. T. Tallakstad, E. G. Flekkøy, A. Hansen and K. J. Måløy, Film Flow Dominated Simultaneous Flow of Two Viscous Incompressible Fluids Through a Porous Medium , *Front. Phys.* **2**, 63 (2014); doi:10.3389/fphy.2014.00063.
- [27] S. Sinha, A. T. Bender, M. Danczyk, K. Keepseagle, C. A. Prather, J. M. Bray, L. W. Thrane, J. D. Seymour, S. L. Codd and A. Hansen, Effective Rheology of Two-Phase Flow in Three-Dimensional Porous Media: Experiment and Simulation, *Transp. Porous Med.* **119**, 77-94 (2017); doi.org/10.1007/s11242-017-0874-4.
- [28] Y. Gao, Q. Lin, B. Bijeljic and M. J. Blunt, Pore-scale dynamics and the multiphase Darcy law, *Phys. Rev. Fluids*, **5**, 013801 (2020); doi.org/10.1103/PhysRevFluids.5.013801.
- [29] Y. Zhang, B. Bijeljic, Y. Gao, Q. Lin and M. J. Blunt, Quantification of Nonlinear Multiphase Flow in Porous Media, *Geophys. Res. Lett.* **48**, e2020GL090477 (2021); doi.org/10.1029/2020GL090477.
- [30] S. Sinha and A. Hansen, Effective rheology of immiscible two-phase flow in porous media, *EPL*, **99**, 44004 (2012); doi.org/10.1209/0295-5075/99/44004.
- [31] S. Sinha, A. Hansen, D. Bedeaux and S. Kjelstrup, Effective Rheology of Bubbles Moving in a Capillary Tube , *Phys. Rev. E* **87**, 025001 (2013); doi:10.1103/PhysRevE.87.025001.
- [32] X. Xu and X. Wang, Non-Darcy behavior of two-phase channel flow, *Phys. Rev. E*, **90**, 023010 (2014); doi.org/10.1103/PhysRevE.90.023010.
- [33] A. G. Yiotis, A. Dollari, M. E. Kainourgiakis, D. Salin, and L. Talon, Nonlinear Darcy flow dynamics during ganglia stranding and mobilization in heterogeneous porous domains *Phys. Rev. Fluids* **4**, 114302 (2019); doi.org/10.1103/PhysRevFluids.4.114302.
- [34] S. Roy, S. Sinha and A. Hansen, Effective rheology of two-phase flow in a capillary fiber bundle model, *Front. Phys.* **7**, 92 (2019); doi.org/10.3389/fphy.2019.00092.
- [35] S. Roy, S. Sinha and A. Hansen, Effective rheology in the continuum limit, arXiv:1912.05248.
- [36] F. Lanza, A. Hansen, A. Rosso and L. Talon, Non-Newtonian rheology in a capillary tube with varying radius, arXiv:2106.04325.
- [37] H. Fyhn, S. Sinha, S. Roy and A. Hansen, Rheology of immiscible two-phase flow in mixed wet porous media: Dynamic pore network model and capillary fiber bundle model results, arXiv:2105.07486.

- [38] V. Joekar-Niasar and S. M. Hassanizadeh, Analysis of Fundamentals of Two-Phase Flow in Porous Media Using Dynamic Pore-Network Models: a Review, *Crit. Rev. Environ. Sc. Tech.* **42**, 1895 (2012); doi:10.1080/10643389.2011.574101.
- [39] E. Aker, K. J. Måløy, A. Hansen and G. G. Batrouni, A Two-Dimensional Network Simulator for Two-Phase Flow in Porous Media, *Transp. Porous Media*, **32**, 163 (1998), doi:10.1023/A:1006510106194.
- [40] M. Aa. Gjennestad, M. Vassvik, S. Kjelstrup and A. Hansen, Stable and Efficient Time Integration of a Dynamic Pore Network Model for Two-Phase Flow in Porous Media, *Front. Phys.* **6**, 56 (2018); doi.org/10.3389/fphy.2018.00056.
- [41] M. Aa. Gjennestad, M. Winkler and A. Hansen, Pore Network Modeling of the Effects of Viscosity Ratio and Pressure Gradient on Steady-State Incompressible Two-Phase Flow in Porous Media, *Transp. Porous Media*, **132**, 355 (2020); doi.org/10.1007/s11242-020-01395-z.
- [42] S. Sinha, M. Aa. Gjennestad, M. Vassvik and A. Hansen, Fluid meniscus algorithms for dynamic pore-network modeling of immiscible two-phase flow in porous media, *Front. Phys.* **8**, 548497 (2020); doi.org/10.3389/fphy.2020.548497.
- [43] H. A. Knudsen and A. Hansen, Two-phase flow in porous media: dynamical phase transition, *Eur. Phys. J. B*, **49**, 109 (2006); doi:10.1140/epjb/e2006-00019-y.
- [44] J. Bear and Y. Bachmat, *Introduction to modeling of transport phenomena in porous media*, (Springer, Berlin, 2012); doi:10.1007/978-94-009-1926-6.
- [45] A. Aharony and A. B. Harris, Absence of self-averaging and universal fluctuations in random systems near critical points, *Phys. Rev. Lett.* **77**, 3700 (1996); doi:10.1103/PhysRevLett.77.3700.
- [46] J. Feder, E. G. Flekkøy and A. Hansen, *Physics of Flow in Porous Media* (Cambridge University Press, Cambridge, 2022). (In print.)
- [47] M. Erpelding, S. Sinha, K. T. Tallakstad, A. Hansen, E. G. Flekkøy, and K. J. Måløy, History independence of steady state in simultaneous two-phase flow through two-dimensional porous media, *Phys. Rev. E*, **88**, 053004 (2013); doi:10.1103/PhysRevE.88.053004.
- [48] M. S. Valavanides, Oil Fragmentation, Interfacial Surface Transport and Flow Structure Maps for Two-Phase Flow in Model Pore Networks. Predictions Based on Extensive, DeProF Model Simulations, *Oil and Gas Sci. Tech. Rev. IFP Energies nouvelles*, **73**, (6) (2018); doi:doi.org/10.2516/ogst/2017033.
- [49] B. Bennion and S. Bachu, Relative permeability characteristics for supercritical CO<sub>2</sub> displacing water in a variety of potential sequestration zones, *SPE Annual Technical Conference and Exhibition* (2005); doi.org/10.2118/95547-MS.
- [50] R. Fulcher, T. Ertekin and C. Stahl, Effect of capillary number and its constituents on two-phase relative permeability curves, *J. Petr. Tech.* **37**, 249 (1985); doi:10.2118/12170-PA.
- [51] M. Oak, L. Baker and D. Thomas, Three-phase relative permeability of Berea sandstone, *J. of Petr. Tech.* **42**, 1054 (1990); doi.org/10.2118/17370-pa.
- [52] G. Virnovsky, K. Vatne, S. Skjaeveland and A. Lohne, Implementation of multirate technique to measure relative permeabilities accounting, *SPE Annual Technical Conference and Exhibition. OnePetro* (1998); doi.org/10.2118/49321-MS.
- [53] C. A. Reynolds and S. Krevor, Characterizing flow behavior for gas injection: Relative permeability of CO<sub>2</sub>-brine and N<sub>2</sub>-water in heterogeneous rocks, *Water Res. Res.* **51**, 9464 (2015); doi.org/10.1002/2015wr018046.

- [54] M. Leverett, Flow of oil-water mixtures through unconsolidated sands, Trans. of the AIME **132**, 149 (1939); doi.org/10.2118/939149-g.
- [55] A. Rohatgi, Webplotdigitizer: Version 4.4 (2020), <https://automeris.io/WebPlotDigitizer>.
- [56] E. W. Washburn, The Dynamics of Capillary Flow, Phys. Rev. **17**, 273 (1921); doi.org/10.1103/PhysRev.17.273.
- [57] G. G. Batrouni and A. Hansen, Fourier Acceleration of Iterative Processes in Disordered Systems, J. Stat. Phys. **52**, 747 (1988); doi.org/10.1007/BF01019728.